

Molecular light-upconversion: we have had a problem! When excited state absorption (ESA) overcomes energy transfer upconversion (ETU) in Cr(III)/Er(III) complexes

Bahman Golesorkhi,* Inès Taarit, Hélène Bolvin,* Homayoun Nozary, Juan-Ramón Jiménez, Céline Besnard, Laure Guénée, Alexandre Fürstenberg, and Claude Piguet*

Supporting Information

(51 pages)

Table of contents

Experimental section	S2-S7
Kinetic Matrices	S8
Speciation in solution	S9
X-Ray crystallography	S10-S18
Crystal field parameters	S19-S23
Photophysical data	S24-S51

Experimental Section

Solvents and starting materials

Solvents and starting materials were purchased from Strem, Acros, Fluka AG and Aldrich and used without further purification unless otherwise stated. $\text{Er}(\text{ClO}_4)_3 \cdot x\text{H}_2\text{O}$ and $\text{Er}(\text{CF}_3\text{SO}_3)_3 \cdot x\text{H}_2\text{O}$ were prepared from the corresponding oxides (Aldrich, 99.99%).^{S1} The Ln content of solid salts was determined by complexometric titrations with Titriplex III (Merck) in the presence of urotropine and xylene orange.^{S2} The commercially available dipicolinic acid (dpa) was used for the synthesis of Er(III) complexes. The ligands dipicolinic acid-diethyl ester (dpa-ester)^{S3} and *N,N,N'N'*-tetraethyldipicolinamide (dpa-amide)^{S4} and the complexes $[\text{Er}(\text{Et-bzimpy})_3](\text{ClO}_4)_3 \cdot 2\text{CH}_3\text{CN}$,^{S5} $[\text{Er}(\text{tpy})_3](\text{ClO}_4)_3$,^{S5} $[\text{Er}(\text{Et-tpy})_3](\text{ClO}_4)_3 \cdot 1.5\text{CH}_3\text{CN}$ ^{S5} and $[\text{GaErGa}(\text{bpb-bzimpy})_3]_2(\text{CF}_3\text{SO}_3)_{18} \cdot 30\text{C}_3\text{H}_5\text{N}$ ^{S6} were prepared according to literature procedures. Acetonitrile and dichloromethane were distilled over calcium hydride.

Preparation of $(\text{HNEt}_3)_5[\text{Er}(\text{dpa})_3](\text{CF}_3\text{SO}_3)_2$ (1). To a solution of the ligand dpa (131 mg, 0.78 mmol, 3.0 eq) in methanol (10 mL), triethylamine (300 mg, 2.96 mmol, 6 eq) was added dropwise. A solution of $[\text{Er}(\text{CF}_3\text{SO}_3)_3] \cdot x\text{H}_2\text{O}$ (367 mg, 0.60 mmol, 1.0 eq) in acetonitrile (5 mL) was then added to the solution of ligand and the reaction mixture was stirred for 2 h at room temperature. The resulting mixture was filtered and its volume reduced under reduced pressure. The solid residue was dissolved in a minimum amount of butyronitrile. Slow diffusion of diethyl ether provided crystals of $(\text{HNEt}_3)_5[\text{Er}(\text{dpa})_3](\text{CF}_3\text{SO}_3)_2$ (**1**, 606 mg, yield: 69 %) suitable for X-ray diffraction studies. Separation from the mother liquor followed by air drying gave satisfying elemental analysis for $[\text{Er}(\text{dpa})_3](\text{HN}(\text{CH}_3\text{CH}_2)_3)_5(\text{CF}_3\text{SO}_3)_2 \cdot 2\text{CH}_3\text{OH}$ (calcd C 43.01, H 6.37, N 7.30; found C 42.37, H 6.07, N 7.31).

Preparation of $[\text{Er}(\text{dpa-ester})_3](\text{ClO}_4)_3$ (2). $[\text{Er}(\text{ClO}_4)_3] \cdot x\text{H}_2\text{O}$ (162.5 mg, 0.225 mmol, 1.0 eq) in acetonitrile (5 mL) was added into a 5 mL acetonitrile solution of dpa-ester (150 mg, 0.67 mmol, 3.0 eq) upon stirring at room temperature. The volume of the resulting solution was reduced under reduced pressure without warming, and the solid residue was dissolved in a minimum amount of butyronitrile. Slow diffusion of diethyl ether into the later solution provided crystals of $[\text{Er}(\text{dpa-ester})_3](\text{ClO}_4)_3$ (**2**, 150 mg, yield: 63 %) suitable for X-ray diffraction studies. Separation from the mother liquor followed by air drying gave satisfying elemental analysis for $[\text{Er}(\text{dpa-ester})_3](\text{ClO}_4)_3 \cdot 0.6\text{C}_3\text{H}_7\text{CN} \cdot 1.05\text{C}_4\text{H}_{10}\text{O}$ (calcd C 34.48, H 3.59, N 4.31; found C 34.86, H 3.19, N 3.91).

Preparation of $[\text{Er}(\text{dpa-amide})_3](\text{ClO}_4)_3$ (3). $[\text{Er}(\text{ClO}_4)_3] \cdot x\text{H}_2\text{O}$ (325 mg, 0.45 mmol, 1.0 eq) in acetonitrile (5 mL) was added to a 5 mL acetonitrile solution of the dpa-amide (373 mg, 1.34 mmol, 3.0 eq) upon stirring at room temperature. The volume of resulting solution was reduced under

reduced pressure without warming, and the solid residue was dissolved in a minimum amount of butyronitrile. Slow diffusion of diethyl ether into the later solution provided crystals of [Er(dpa-amide)₃](ClO₄)₃ (**3**, 440 mg, yield: 75 %) suitable for X-ray diffraction studies. Separation from the mother liquor followed by air drying gave satisfying elemental analysis for [Er(dpa-amide)₃](ClO₄)₃ (calcd C 41.65, H 5.36, N 9.71; found C 41.52, H 5.35, N 9.71).

Spectroscopic and analytical measurements

Solid-state luminescence data were collected on samples mounted directly onto copper plates using conductive silver glue. Emission spectra were measured on a Horiba Scientific Fluorolog 3 spectrofluorimeter equipped with a visible photomultiplier tube (PMT) (220-850 nm, R928P, Hamamatsu). The infrared luminescence spectra were recorded using either a NIR solid-state InGaAs detector cooled to 77 K (800-1600 nm, DSS-IGA020L; Horiba Scientific) or a NIR-PMT cooled to -80 °C (300-1700 nm, R5509-73, Hamamatsu) and a 850 nm longpass filter (Semrock) upon 801 nm laser excitation. The low-temperature emission spectra were recorded using an optical closed-cycle cryostat capable of reaching low temperatures down to 5 K in a helium atmosphere (Sumitomo HC-4E/Janis Research CCS-900/204N). The emission spectra were corrected for the instrumental response function. Resonant excitations into the Er(⁴I_{9/2} ← ⁴I_{15/2}) and Er(⁴I_{11/2} ← ⁴I_{15/2}) transitions in Er(III) complexes were achieved respectively with diode lasers MLL-H-800-2.5W (801 nm) and MDL-F-980-10W (966 nm) from Changchun New Industries Optoelectronics Technology Co., Ltd (CNI). A 550/88 nm bandpass filter (Semrock) was placed directly after the sample for visible emission measurements in order to remove the second-order Rayleigh scattering of the laser line. NIR luminescent lifetimes were measured using the excitation provided by a pulsed Nd:YAG laser (Quantel Qsmart 850) equipped with frequency tripler ($\lambda_{\text{exc}} = 355$ nm) and a Quantel Q-scan dye laser (LDS 821 and LDS 925 dyes from Luxottica Exciton for pulsed excitations into the Er(⁴I_{9/2} ← ⁴I_{15/2}) transition at $\lambda_{\text{exc}} = 805$ nm and into the Er(⁴I_{11/2} ← ⁴I_{15/2}) transition at $\lambda_{\text{exc}} = 950$ nm respectively. Any pump laser residual signal was removed at the exit of the Nd:YAG laser with a 650 nm longpass cut-off filter. Pulsed excitations into the Er(⁴I_{11/2} ← ⁴I_{15/2}) transition at $\lambda_{\text{exc}} = 975$ nm was achieved with a pulsed diode laser PDL 800-D from PicoQuant coupled to a pulse generator (MFG-2110, GW Instek) in order to achieve low repetition rates. For time-resolved experiments, the decay curves were recorded from excited samples at 298 K with a photomultiplier (Hamamatsu R2658 or R928) and a digital oscilloscope (Tektronix MDO4104C). The excitation beam was loosely focused onto the sample with a 30 cm focal lens to reach an excitation spot size of ≈ 1.5 mm in diameter (surface ≈ 0.07 cm²). The mathematical analyses were performed by using Igor Pro® (WaveMetrics Inc.), Origin 2017 (OriginLab Corporation) and Excel® (Microsoft) software. The upconversion quantum yields were determined through the

relative method using indocyanine green as the reference (ICG, $\lambda_{\text{exc}} = 801 \text{ nm}$, $\Phi_r = 0.132$ in ethanol at 298 K, $n_{\text{acetonitrile}} = 1.344$).^{S7} Quantitative data for the upconversion process (up) collected in Table 2 were obtained by using indocyanine green (ref) and Eq S1, where Φ is the quantum yield, E is the integrated emission spectrum, A is the absorbance at the excitation wavelength λ , n is the refractive index ($n_{\text{acetonitrile}} = 1.344$ and $n_{\text{ethanol}} = 1.361$), P_{exc} is the power intensity of the excitation source at the excitation wavelength and $h\nu_{\text{exc}}$ is the energy of the incident photon at frequency $\nu_{\text{exc}} = (c/\lambda_{\text{exc}})$ so that $I_{\text{exc}} = P_{\text{exc}}/h\nu_{\text{exc}}$ is the spectral radiant power measuring the incident excitation intensity.

$$\frac{\Phi^{\text{up}}}{\Phi^{\text{ref}}} = \frac{E_{\text{up}}}{E_{\text{ref}}} \cdot \frac{A_{\text{ref}}}{A_{\text{up}}} \cdot \frac{n_{\text{ref}}^2}{n_{\text{up}}^2} \cdot \frac{P_{\text{exc,ref}}}{P_{\text{exc,up}}} \cdot \frac{h\nu_{\text{exc,up}}}{h\nu_{\text{exc,ref}}} \quad (\text{S1})$$

Extreme care were taken for having identical location of the incident beam into the various cells used for the complexes and the reference. Electronic absorption spectra in the visible and NIR regions were recorded at 298 K from acetonitrile (ethanol for ICG) solutions with a Perkin-Elmer Lambda 1050 absorption spectrometer using quartz cell of 10 mm path length. Solution emission spectra were recorded in non-deuterated acetonitrile (non-deuterated ethanol for ICG) using quartz cells of 5 mm path length. The emission spectrum of ICG was recorded upon excitation at $\lambda_{\text{exc}} = 705 \text{ nm}$ using the standard xenon lamp of the Horiba Scientific Fluorolog 3 spectrofluorimeter. The emission spectra were corrected for the instrumental response function.

X-ray crystallography

Summary of crystal data, intensity measurements and structure refinements for complexes $(\text{HNEt}_3)_5[\text{Er}(\text{dpa})_3](\text{CF}_3\text{SO}_3)_2$ (**1**), $[\text{Er}(\text{dpa-ester})_3](\text{ClO}_4)_3$ (**2**), $[\text{Er}(\text{dpa-amide})_3](\text{ClO}_4)_3$ (**3**) were collected in Table S1. Pertinent bond lengths, bond angles and interplanar angles were collected in Tables S2-S7 together with ORTEP views and the pertinent numbering schemes gathered in Figs S2-S4. The crystals were mounted on Hampton cryoloops with protection oil. X-ray data collections were performed with a XtaLAB Synergy-S diffractometer ($\text{Cu}[\text{K}\alpha]$ radiation) equipped with an hybrid pixel hypix arc 150 detector. The structures were solved by using dual space methods in the SHELXT software^{S8}. Full-matrix least-square refinements on F^2 were performed with SHELXL^{S9} within the Olex2 software^{S9}. CCDC 2059291-2059293 contain the supplementary crystallographic data. These data can be obtained free of charge from the Cambridge Crystallographic Data Centre via www.ccdc.cam.ac.uk/.

*(HNEt₃)₅[Er(dpa)₃](CF₃SO₃)₂ (**1**):* One of the triflate is disordered and was refined using two components with restraints (SADI) on distances and displacement parameters (SIMU for atoms closer to 1 Å AND RIGU). Restraints were also used on displacement parameters for two pairs of very close atoms (EADP). Two of the HNEt₃ cations are also disordered and were refined as two

components with geometrical restraints (DFIX DANG) and restraints on displacement parameters. parameters (SIMU for atoms closer to 1 Å AND RIGU). Finally, a column of solvent molecules was remaining and no good modelling of it could be done at our hands. The squeeze/by pass procedure^{S10} implemented in Olex2^{S9} was used. Two voids of 253 Å³ containing 64 electrons each were found. The solvent is a mixed containing CH₃CN, CH₃CH₂CH₂CN, CH₃OH and (CH₃CH₂)₂O. No unambiguous choice from these molecules could be made. The agreement factors before squeezing were *R*1= 4.46 % and *wR*2=12.10%

Computational Details

For all the investigated systems, calculations were performed on the crystallographic structures by using the SO-CASSCF (spin-orbit complete active space self-consistent field) approach. MOLCAS calculations were performed with the MOLCAS (version 7.8) suite of programs.^{S11} Firstly, a SF-CASSCF (spin-free CASSCF) calculation was performed^{S12} with an active space composed of the seven 4f orbitals of the lanthanide ion and 11 associated electrons, that is CAS(11,7). Spin-orbit (SO) coupling was included by a state interaction with the RASSI (restricted active space state interaction) method.^{S13} 35 spin states and 43 doublets were considered for the state interaction. Relativistically contracted ANO (Atomic natural Orbitals) basis sets^{S14} were used with TZP quality for all atoms and DZ for H atoms. Scalar relativistic effects were taken into account by means of the Douglas–Kroll–Hess transformation,^{S15} and the SO integrals were calculated by using the AMFI (atomic mean-field integrals) approximation.^{S16} The g factors were calculated according to Ref. S17 and the CFPs were calculated with a local program written in Mathematica.^{S18} While CASSCF is sufficient to describe the splitting of the states arising from the lowest LS term ⁴I, the inclusion of dynamical correlation is compulsory to describe correctly the other LS terms, which is usually provided by the CASPT2 (Complete Active Space Perturbation Theory at 2nd order) method. Based on the idea that dynamical correlation mostly affects the energy of the LS terms, as a first approach, the SF-CASSCF energies are shifted by the SF-CASPT2 energy of the corresponding LS term of the free ion. Namely, for a state from the LS manifold: $\tilde{E}_I = E_I^{CASSCF} + E_{LS}^{CASPT2} - E_{LS}^{CASSCF}$. The $E_{LS}^{CASPT2} - E_{LS}^{CASSCF}$ values in cm⁻¹ are the following : ⁴F, ⁴S -2330 ; ⁴G -2990 ; ⁴D -4820 ; ²H -1180 ; ²G -1623 ; ²J -1030. This approach was successfully compared to the full CASPT2 performed on the [Er(dpa)₃]³⁻ complex. It will be denoted SO-CASSCF(PT2shift) in the following of the text.

We followed the work by Bernadotte *et al.* to evaluate the different contributions to the oscillator strength, up to first order in the multipole expansion.^{S19} For the first order term to be origin independent, crossed electric-dipole-electric-octupole and electric-dipole-magnetic-quadrupole contributions should be considered. But since the origin dependence of the magnetic-dipole transition moments vanishes if the electric-dipole transition moment is zero, we neglected the

crossed contributions, and considered the origin of the angular magnetic moment located at the Er atom.

The electric-dipole contribution to the oscillator strength for transition $i \rightarrow j$ was calculated according to

$$f_{ij}^{(\mu^2)} = \frac{2m_e}{3e^2\hbar^2} E_{ij} \sum_{\alpha=x,y,z} \langle i | \hat{\mu}_\alpha | j \rangle^2$$

where m_e and e are the mass and the charge of the electron, \hbar is the reduced Planck constant. E_{ij} is the energy gap and $\hat{\mu}_\alpha$ is component α of the electric-dipole operator. The magnetic-dipole contribution writes:

$$f_{ij}^{(m^2)} = \frac{2m_e}{3e^2\hbar^2c^2} E_{ij} \sum_{\alpha=x,y,z} [\text{Im} \langle i | \hat{m}_\alpha | j \rangle]^2$$

where c is the speed of light and \hat{m}_α is component α of the magnetic-dipole operator. The electric-quadrupole contribution was calculated as

$$f_{ij}^{(Q^2)} = \frac{m_e}{10e^2\hbar^4c^2} E_{ij}^3 \left[\sum_{\alpha,\beta=x,y,z} \langle i | \hat{Q}_{\alpha\beta} | j \rangle^2 - \frac{1}{3} \sum_{\alpha} \langle i | \hat{Q}_{\alpha\alpha} | j \rangle^2 \right]$$

where $\hat{Q}_{\alpha\beta}$ is component $\alpha\beta$ of the electric-quadrupole operator. The oscillator strength between two manifolds $I \rightarrow J$ where the thermal equilibrium is reached in the absorbing manifold I was evaluated as follows

$$f_{IJ} = \sum_{i \in I; j \in J} f_{ij} e^{-\frac{E_i - E_j^0}{k_B T}}$$

where k_B is the Boltzmann constant, T the temperature and E_i^0 the energy of the lowest state of manifold I .

References

- S1 J. F. Desreux, in *Lanthanide Probes in Life, Chemical and Earth Sciences* (Eds: J.-C. G. Bünzli, G. R. Choppin), Elsevier, Amsterdam, 1989
- S2 G. Schwarzenbach, *Complexometric Titrations*, Chapman & Hall, London, 1957
- S3 F. Renaud, C. Piguet, G. Bernardinelli, J.-C. G. Bünzli and G. Hopfgartner, *Chem. Eur. J.*, 1997, **3**, 1660-1667.
- S4 F. Renaud, C. Piguet, G. Bernardinelli, J.-C.-G. Bünzli and G. Hopfgartner, *Chem. Eur. J.*, 1997, **3**, 1646-1659.
- S5 B. Golesorkhi, L. Guénée, H. Nozary, A. Fürstenberg, Y. Suffren, S. V. Eliseeva, S. Petoud, A. Hauser and C. Piguet, *Chem. Eur. J.*, 2018, **24**, 13158-13169.

- S6 a) L. Aboshyan-Sorgho, C. Besnard, P. Pattison, K. R. Kittilstved, A. Aebsicher, J.-C. G. Bünzli, A. Hauser and C. Piguet, *Angew. Chem. Int. Ed.*, 2011, **50**, 4108-4112; b) D. Zare, Y. Suffren, L. Guénée, S. V. Eliseeva, H. Nozary, L. Aboshyan-Sorgho, S. Petoud, A. Hauser and C. Piguet, *Dalton Trans.*, 2015, **44**, 2529-2540.
- S7 a) K. Rurack and M. Spieles, *Analytical Chemistry*, 2011, **83**, 1232-1242; b) C. Wurth, M. Grabolle, J. Pauli, M. Spieles and U. Resch-Genger, *Nature Protocols*, 2013, **8**, 1535-1550; c) N. Souri, P. Tian, C. Platas-Iglesias, K.-L. Wong, A. Nonat and L. J. Charbonnière, *J. Am. Chem. Soc.*, 2017, **139**, 1456-1459; d) A. Nonat, S. Bahamyrou, A. Lecointre, F. Przybilla, Y. Mély, C. Platas-Iglesias, F. Camerel, O. Jeannin and L. J. Charbonnière, *J. Am. Chem. Soc.*, 2019, **141**, 1568-1576.
- S8 G. M. Sheldrick, *Acta Cryst. A*, 2015, **71**, 3–8.
- S9 O. V. Dolomanov, L. J. Bourhis, R. J. Gildea, J. A. K. Howard and H. Puschmann, *J. Appl. Cryst.*, 2009, **42**, 339–341.
- S10 P. van der Sluis and A. L. Spek, *Acta Cryst. A*, 1990, **46**, 194–201.
- S11 F. Aquilante, L. De Vico, N. Ferré, G. Ghigo, P.-A. Malmqvist, P. Neogràdy, T. B. Pedersen, M. Pitonak, M. Reiher, B. O. Roos, M. Serrano Andrés, M. Urban, V. Veryazov and R. Lindh, *J. Comput. Chem.*, 2010, **31**, 224.
- S12 B. O. Roos, P. R. Taylor and P. E. M. Siegbahn, *Chem. Phys.*, 1980, **48**, 157.
- S13 P.-A. Malmqvist, B. O. Roos and B. Schimmelpfennig, *Chem. Phys. Lett.*, 2002, **357**, 230.
- S14 a) B. O. Roos, R. Lindh, P.-A. Malmqvist, V. Veryazov and P.-O. Widmark, *J. Phys. Chem. A*, **2004**, *108*, 2851-2858; b) B. O. Roos, R. Lindh, P.-A. Malmqvist, V. Veryazov and P.-O. Widmark, *Chem. Phys. Lett.*, 2005, **409**, 295-299.
- S15 B. A. Hess, *Phys. Rev. A*, 1986, **33**, 3742.
- S16 B. A. Hess, C. M. Marian, U. Wahlgren and O. A. Gropen, *Chem. Phys. Lett.*, 1996, **251**, 365.
- S17 H. Bolvin, *ChemPhysChem*, 2006, **7**, 1575-1589.
- S18 J. Jung, M. A. Islam, V. L. Pecoraro, T. Mallah, C. Berthon and H. Bolvin, *Chem. Eur. J.*, 2019, **25**, 15112-15122.
- S19 S. Bernadotte, A. J. Atkins and C. R. Jacob, *J. Chem. Phys.*, 2012, **137**, 204106,

a) ESA mechanism (Figure 1)

$$\begin{pmatrix} dN_A^{(0)} / dt \\ dN_A^{(1)} / dt \\ dN_A^{(2)} / dt \end{pmatrix} = \begin{pmatrix} -k_A^{\text{exc}(0 \rightarrow 1)} & k_A^{1 \rightarrow 0} & k_A^{2 \rightarrow 0} \\ k_A^{\text{exc}(0 \rightarrow 1)} & -(k_A^{\text{exc}(1 \rightarrow 2)} + k_A^{1 \rightarrow 0}) & k_A^{2 \rightarrow 1} \\ 0 & k_A^{\text{exc}(1 \rightarrow 2)} & -(k_A^{2 \rightarrow 1} + k_A^{2 \rightarrow 0}) \end{pmatrix} \times \begin{pmatrix} N_A^{(0)} \\ N_A^{(1)} \\ N_A^{(2)} \end{pmatrix}$$

b) ETU mechanism (Figure 3)

$$\begin{pmatrix} dN_{\text{SAS}}^{(0)} / dt \\ dN_{\text{SAS}}^{(1)} / dt \\ dN_{\text{SAS}}^{(2)} / dt \\ dN_{\text{SAS}}^{(3)} / dt \\ dN_{\text{SAS}}^{(4)} / dt \\ dN_{\text{SAS}}^{(5)} / dt \end{pmatrix} = \begin{pmatrix} -2k_S^{\text{exc}(0 \rightarrow 1)} & k_S^{1 \rightarrow 0} & 0 & k_A^{1 \rightarrow 0} & 0 & k_A^{2 \rightarrow 0} \\ 2k_S^{\text{exc}(0 \rightarrow 1)} & -\begin{pmatrix} k_S^{\text{exc}(0 \rightarrow 1)} \\ +k_S^{1 \rightarrow 0} \\ +W_{\text{S} \rightarrow \text{A}}^1 \end{pmatrix} & 2k_S^{1 \rightarrow 0} & 0 & k_A^{1 \rightarrow 0} & 0 \\ 0 & k_S^{\text{exc}(0 \rightarrow 1)} & -\begin{pmatrix} 2k_S^{1 \rightarrow 0} \\ 2W_{\text{S} \rightarrow \text{A}}^1 \end{pmatrix} & 0 & 0 & 0 \\ 0 & W_{\text{S} \rightarrow \text{A}}^1 & 0 & -\begin{pmatrix} 2k_S^{\text{exc}(0 \rightarrow 1)} \\ +k_A^{1 \rightarrow 0} \end{pmatrix} & k_S^{1 \rightarrow 0} & k_A^{2 \rightarrow 1} \\ 0 & 0 & 2W_{\text{S} \rightarrow \text{A}}^1 & 2k_S^{\text{exc}(0 \rightarrow 1)} & -\begin{pmatrix} k_S^{1 \rightarrow 0} \\ +k_A^{1 \rightarrow 0} \\ W_{\text{S} \rightarrow \text{A}}^2 \end{pmatrix} & 0 \\ 0 & 0 & 0 & 0 & W_{\text{S} \rightarrow \text{A}}^2 & -\begin{pmatrix} k_A^{2 \rightarrow 0} \\ +k_A^{2 \rightarrow 1} \end{pmatrix} \end{pmatrix} \times \begin{pmatrix} N_{\text{SAS}}^{(0)} \\ N_{\text{SAS}}^{(1)} \\ N_{\text{SAS}}^{(2)} \\ N_{\text{SAS}}^{(3)} \\ N_{\text{SAS}}^{(4)} \\ N_{\text{SAS}}^{(5)} \end{pmatrix}$$

Scheme S1 Kinetic matrix for a) the ESA mechanism for a single-center activator depicted in Figure 1 and b) the ETU mechanism for a SAS triad as shown in Figure 3.

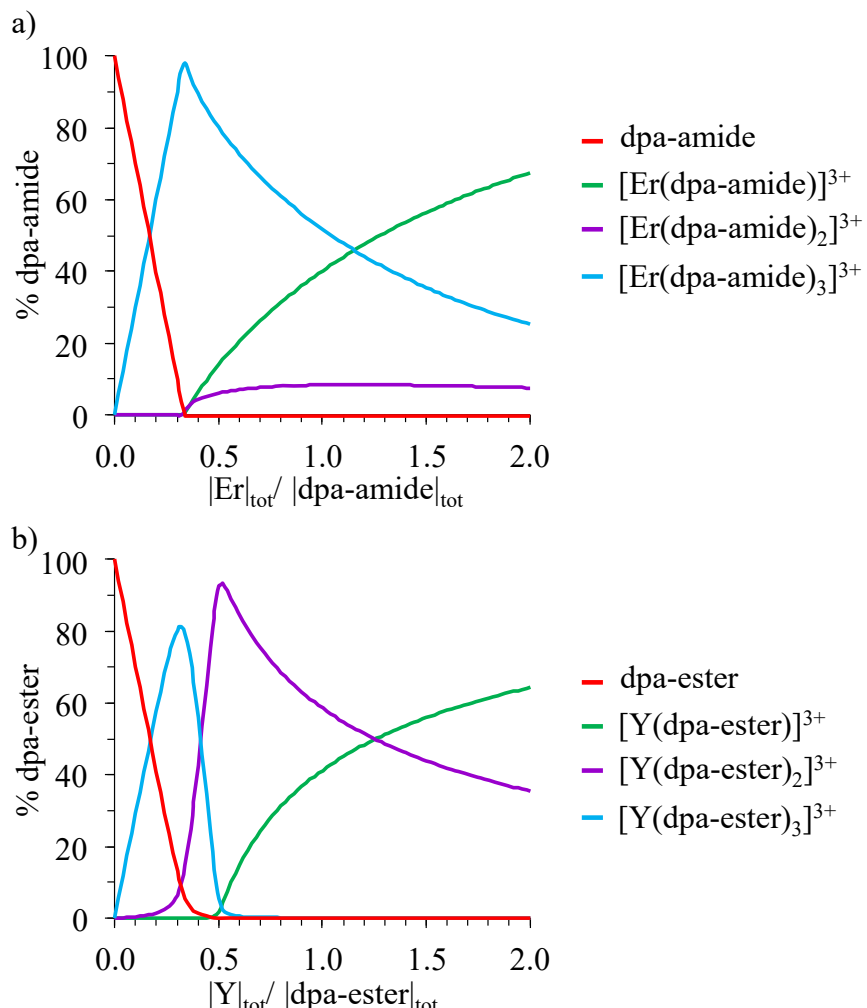


Figure S1 Macroscopic speciation curves computed for the titrations of ligand a) dpa-amide and b) dpa-ester with Ln(III) (Ln = Er for dpa-amide and Y for dpa-ester) for $|\text{dpa-amide}|_{\text{tot}} = |\text{dpa-ester}|_{\text{tot}} = 1 \times 10^{-2} \text{ mol} \cdot \text{dm}^{-3}$ and using the stability constants $\log(\beta_{1,1}^{\text{Er,dpa-amide}}) = 7.7(4)$, $\log(\beta_{1,2}^{\text{Er,dpa-amide}}) = 14.4(4)$ and $\log(\beta_{1,3}^{\text{Er,dpa-amide}}) = 22.7(4)$ ^[30] and $\log(\beta_{1,1}^{\text{Y,dpa-ester}}) = 6.9(4)$, $\log(\beta_{1,2}^{\text{Y,dpa-ester}}) = 13.5(4)$ and $\log(\beta_{1,3}^{\text{Y,dpa-ester}}) = 17.3(4)$.^[29]

Table S1. Summary of crystal data, intensity measurements and structure refinements for complexes $(\text{HNEt}_3)_5[\text{Er}(\text{dpa})_3](\text{CF}_3\text{SO}_3)_2$ (**1**), $[\text{Er}(\text{dpa-ester})_3](\text{ClO}_4)_3$ (**2**) and $[\text{Er}(\text{dpa-amide})_3](\text{ClO}_4)_3$ (**3**).

	$(\text{HNEt}_3)_5[\text{Er}(\text{dpa})_3](\text{CF}_3\text{SO}_3)_2$	$[\text{Er}(\text{dpa-ester})_3](\text{ClO}_4)_3$	$[\text{Er}(\text{dpa-amide})_3](\text{ClO}_4)_3$
Empirical formula	$\text{C}_{53}\text{H}_{89}\text{ErF}_6\text{N}_8\text{O}_{18}\text{S}_2$	$\text{C}_{33}\text{H}_{39}\text{Cl}_3\text{ErN}_3\text{O}_{24}$	$\text{C}_{45}\text{H}_{69}\text{Cl}_3\text{ErN}_9\text{O}_{18}$
Formula weight	1471.70	1135.28	1297.70
Temperature	149.99(10) K	150.0(1) K	150.0(1) K
Wavelength	1.54184 Å	1.54184 Å	1.54184 Å
Crystal System, Space group	Orthorhombic, $P2_1P2_1P2_1$ $a = 12.07717(9)$ Å $b = 23.7428(2)$ Å	Monoclinic, $P121/c1$ $c = 26.7999(2)$ Å $\alpha = 90^\circ$ $\beta = 93.2566(8)^\circ$ $\gamma = 90^\circ$	Monoclinic, $C121/c1$ $a = 23.2795(1)$ Å $b = 12.8961(1)$ Å $c = 36.9800(2)$ Å $\alpha = 90^\circ$ $\beta = 91.5950(4)^\circ$ $\gamma = 90^\circ$
Unit cell dimensions	$c = 24.7043(2)$ Å $\alpha = 90^\circ$ $\beta = 90^\circ$ $\gamma = 90^\circ$		
Volume in Å ³	7083.87(11)	4382.14(8)	11097.6(1)
Z, Calculated density	4, 1.380 Mg/m ³	4, 1.721 Mg/m ³	8, 1.553 Mg/m ³
Absorption coefficient	3.462 mm ⁻¹	6.045 mm ⁻¹	4.797 mm ⁻¹
$F(000)$	3044	2276	5320
Theta range for data collection	2.581 to 71.207° -14≤=h≤=13, -29≤=k≤=27, -29≤=l≤=30	3.303 to 74.369° -15≤=h≤=14, -15≤=k≤=15, -30≤=l≤=33	2.391 to 74.803° -29≤=h≤=25, -16≤=k≤=15, -45≤=l≤=46
Limiting indices			
Reflections collected / unique	56119 / 13503 [$R(\text{int}) = 0.0496$]	57958 / 8746 [$R(\text{int}) = 0.0290$]	60481 / 11246 [$R(\text{int}) = 0.0248$]
Completeness to theta	67.684° / 99.8 %	67.684° / 99.1 %	67.654° / 99.7 %
Data / restraints / parameters	13503 / 376 / 922	8746 / 87 / 598	11246 / 0 / 721
Goodness-of-fit on F^2	1.039	1.063	1.038
Final R indices [$I > 2\sigma(I)$]	$R_1 = 0.0365$, $\omega R_2 = 0.0932$	$R_1 = 0.0333$, $\omega R_2 = 0.0892$	$R_1 = 0.0317$, $\omega R_2 = 0.0790$
R indices (all data)	$R_1 = 0.0399$ $\omega R_2 = 0.0948$	$R_1 = 0.0380$, $\omega R_2 = 0.0921$	$R_1 = 0.0333$, $\omega R_2 = 0.0800$
Largest diff. peak and hole	0.573 and -0.827 e·Å ⁻³	0.759 and -0.782 e·Å ⁻³	1.529 and -0.600 e·Å ⁻³

Table S2. Selected bond distances (Å) and bond angles (°) for complex $(\text{HNEt}_3)_5[\text{Er}(\text{dpa})_3](\text{CF}_3\text{SO}_3)_2$ (**1**).

Bond distances (Å)					
Atom 1	Atom 2	Distance	Atom 1	Atom 2	Distance
Er(1)	O(1)	2.393(3)	Er(1)	O(6)	2.399(3)
Er(1)	O(2)	2.329(3)	Er(1)	N(1)	2.447(4)
Er(1)	O(3)	2.366(3)	Er(1)	N(2)	2.480(4)
Er(1)	O(4)	2.392(3)	Er(1)	N(3)	2.478(4)
Er(1)	O(5)	2.388(3)			

Angles (°)			
At. 1	At. 2	At. 3	angle
At. 1	At. 2	At. 3	angle
O(1)	Er(1)	O(4)	78.50(12)
O(1)	Er(1)	O(5)	78.14(12)
O(1)	Er(1)	O(6)	87.04(12)
O(1)	Er(1)	N(1)	65.01(13)
O(1)	Er(1)	N(2)	134.52(13)
O(1)	Er(1)	N(3)	70.75(13)
O(2)	Er(1)	O(1)	130.70(13)
O(2)	Er(1)	O(3)	79.85(12)
O(2)	Er(1)	O(4)	85.68(12)
O(2)	Er(1)	O(5)	144.69(12)
O(2)	Er(1)	O(6)	78.85(12)
O(2)	Er(1)	N(1)	65.72(13)
O(2)	Er(1)	N(2)	73.89(13)
O(2)	Er(1)	N(3)	136.83(12)
O(3)	Er(1)	O(1)	143.77(12)
O(3)	Er(1)	O(4)	129.35(12)
O(3)	Er(1)	O(5)	83.88(12)
O(3)	Er(1)	O(6)	80.06(12)
O(3)	Er(1)	O(1)	143.77(12)
O(3)	Er(1)	O(4)	129.35(12)
O(3)	Er(1)	O(5)	83.88(12)
O(3)	Er(1)	O(6)	80.06(12)
O(3)	Er(1)	N(1)	122.24(13)
O(3)	Er(1)	N(2)	138.41(13)
O(3)	Er(1)	N(3)	63.93(12)
N(1)	Er(1)	N(2)	116.95(13)
N(1)	Er(1)	N(3)	120.79(13)

Table S3. Selected least-squares planes data for complex $(\text{HNEt}_3)_5[\text{Er}(\text{dpa})_3](\text{CF}_3\text{SO}_3)_2$ (**1**).

Least-squares planes

Least-squares planes description	Abbreviation	Max. deviation/ \AA	Atom
Pyridine 1 N(1) C(2) C(3) C(4) C(5) C(6)	Py1	0.017	C(3)
Pyridine 2 N(2) C(53) C(10) C(11) C(12) C(13)	Py2	0.015	C(11)
Pyridine 3 N(3) C(16) C(17) C(18) C(19) C(20)	Py3	0.006	C(10)

Interplanar angles ($^{\circ}$)

	Py1	Py2	Py3
Py1		90.5(2)	100.8(2)
Py2			78.5(2)

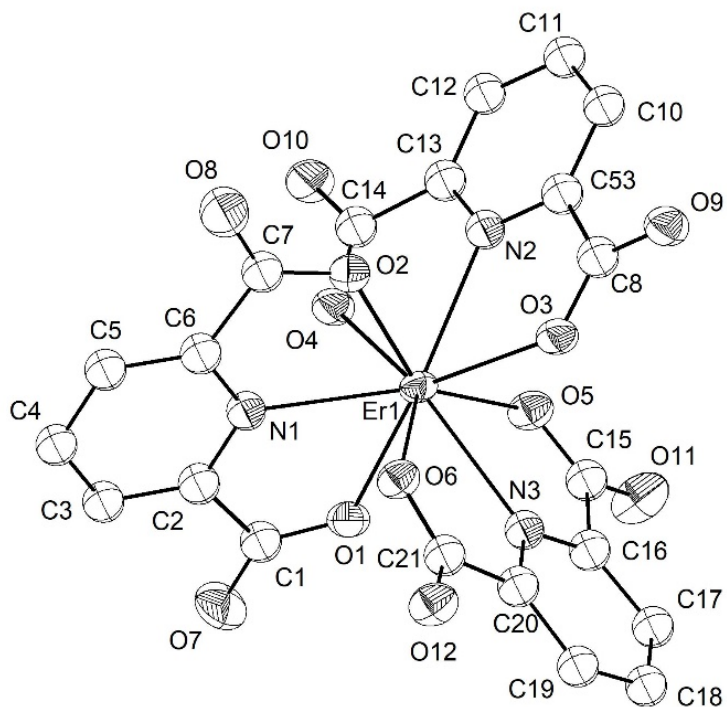
**Figure S2.** ORTEP molecular view with numbering scheme of the asymmetric unit of $[\text{Er}(\text{dpa})_3]^{3-}$ in the crystal structure of $(\text{HNEt}_3)_5[\text{Er}(\text{dpa})_3](\text{CF}_3\text{SO}_3)_2$ (**1**). Thermal ellipsoids are represented at 50% probability level and hydrogen atoms are omitted for clarity.

Table S4. Selected bond distances (\AA) and bond angles ($^\circ$) for complex $[\text{Er}(\text{dpa-ester})_3](\text{ClO}_4)_3$ (2).

Bond distances (\AA)

Atom 1	Atom 2	Distance	Atom 1	Atom 2	Distance
Er(1)	O(1)	2.386(2)	Er(1)	O(10)	2.394(2)
Er(1)	O(2)	2.383(2)	Er(1)	N(1)	2.448(2)
Er(1)	O(5)	2.386(2)	Er(1)	N(2)	2.446(2)
Er(1)	O(6)	2.399(2)	Er(1)	N(3)	2.444(2)
Er(1)	O(9)	2.406(2)			

Angles ($^\circ$)

At. 1	At. 2	At. 3	angle	At. 1	At. 2	At. 3	angle
O(1)	Er(1)	O(6)	147.19(7)	O(5)	Er(1)	N(1)	79.70(7)
O(1)	Er(1)	O(9)	72.13(7)	O(5)	Er(1)	N(2)	65.93(8)
O(1)	Er(1)	O(10)	90.68(7)	O(5)	Er(1)	N(3)	134.66(8)
O(1)	Er(1)	N(1)	65.12(7)	O(6)	Er(1)	O(9)	98.53(7)
O(1)	Er(1)	N(2)	135.42(8)	O(6)	Er(1)	N(1)	128.91(7)
O(1)	Er(1)	N(3)	76.80(8)	O(6)	Er(1)	N(2)	64.40(7)
O(2)	Er(1)	O(1)	129.89(7)	O(6)	Er(1)	N(3)	70.88(8)
O(2)	Er(1)	O(5)	87.94(7)	O(9)	Er(1)	N(1)	132.32(8)
O(2)	Er(1)	O(6)	74.57(7)	O(9)	Er(1)	N(2)	72.17(8)
O(2)	Er(1)	O(9)	146.82(8)	O(9)	Er(1)	N(3)	65.09(8)
O(2)	Er(1)	O(10)	79.05(7)	O(10)	Er(1)	O(6)	71.19(7)
O(2)	Er(1)	N(1)	65.10(7)	O(10)	Er(1)	O(9)	130.30(7)
O(2)	Er(1)	N(2)	75.74(7)	O(10)	Er(1)	N(1)	71.49(7)
O(2)	Er(1)	N(3)	136.66(8)	O(10)	Er(1)	N(2)	133.18(8)
O(5)	Er(1)	O(1)	78.03(7)	O(10)	Er(1)	N(3)	65.66(8)
O(5)	Er(1)	O(6)	129.96(7)	N(1)	Er(1)	N(2)	128.23(8)
O(5)	Er(1)	O(9)	71.55(8)	N(3)	Er(1)	N(1)	121.13(8)
O(5)	Er(1)	O(10)	151.16(7)	N(3)	Er(1)	N(2)	110.52(8)

Table S5. Selected least-squares planes data for complex $[\text{Er}(\text{dpa-ester})_3](\text{ClO}_4)_3$ (**2**).

Least-squares planes

Least-squares planes description	Abbreviation	Max. deviation/ \AA	Atom
Pyridine 1 N(1) C(4) C(5) C(6) C(7) C(8)	Py1	0.007	N(1),C(6)
Pyridine 2 N(2) C(15) C(16) C(17) C(18) C(19)	Py2	0.018	C(19)
Pyridine 3 N(3) C(26) C(27) C(28) C(29) C(30)	Py3	0.007	N3

Interplanar angles ($^{\circ}$)

	Py1	Py2	Py3
Py1		81.6(1)	88.5(1)
Py2			78.2(1)

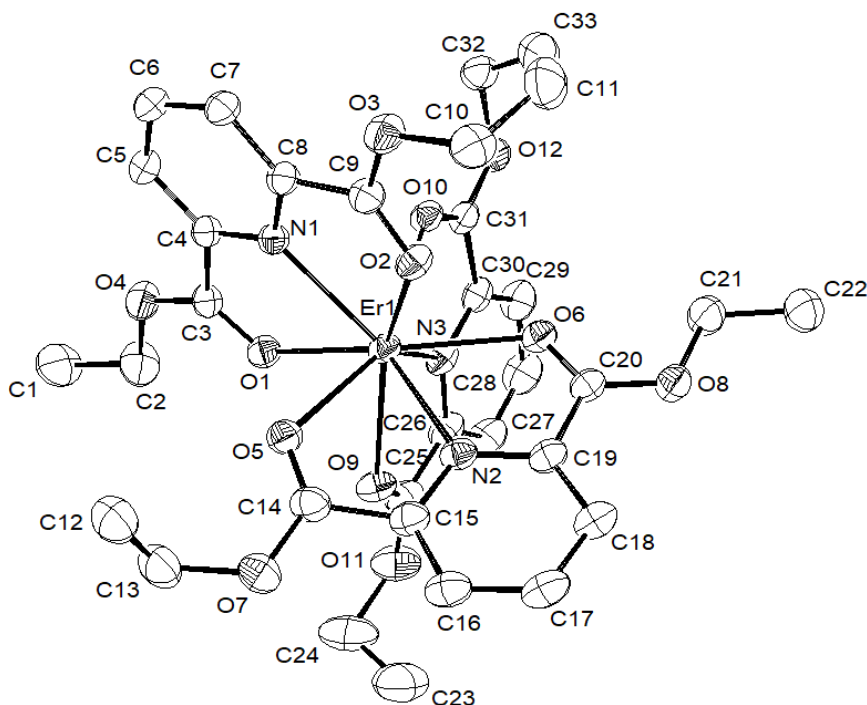
**Figure S3.** ORTEP molecular view with numbering scheme of the asymmetric unit for $[\text{Er}(\text{dpa-ester})_3]^{3+}$ in the crystal structure of $[\text{Er}(\text{dpa-ester})_3](\text{ClO}_4)_3$ (**2**). Thermal ellipsoids are represented at 40% probability level and hydrogen atoms are omitted for clarity.

Table S6. Selected bond distances (Å) and bond angles (°) for complex [Er(dpa-amide)₃](ClO₄)₃ (**3**).

Bond distances (Å)					
Atom 1	Atom 2	Distance	Atom 1	Atom 2	Distance
Er(1)	O(1)	2.380(2)	Er(1)	O(6)	2.322(2)
Er(1)	O(2)	2.345(2)	Er(1)	N(1)	2.496(2)
Er(1)	O(3)	2.378(2)	Er(1)	N(4)	2.480(2)
Er(1)	O(4)	2.341(2)	Er(1)	N(7)	2.515(2)
Er(1)	O(5)	2.355(2)			

Angles (°)			
At. 1	At. 2	At. 3	angle
At. 1	At. 2	At. 3	angle
O(1)	Er(1)	N(1)	65.18(6)
O(1)	Er(1)	N(4)	72.10(6)
O(1)	Er(1)	N(7)	134.19(6)
O(2)	Er(1)	O(1)	130.43(6)
O(2)	Er(1)	O(3)	146.82(6)
O(2)	Er(1)	O(5)	80.75(6)
O(2)	Er(1)	N(1)	65.40(6)
O(2)	Er(1)	N(4)	137.33(6)
O(2)	Er(1)	N(7)	70.34(6)
O(3)	Er(1)	O(1)	75.10(6)
O(3)	Er(1)	N(1)	135.91(6)
O(3)	Er(1)	N(4)	63.64(6)
O(3)	Er(1)	N(7)	76.50(6)
O(4)	Er(1)	O(1)	91.45(6)
O(4)	Er(1)	O(2)	78.02(6)
O(4)	Er(1)	O(3)	127.80(6)
O(4)	Er(1)	O(5)	78.23(6)
O(4)	Er(1)	N(1)	73.22(6)
O(4)	Er(1)	N(4)	64.22(6)
O(4)	Er(1)	N(7)	134.31(6)
O(5)	Er(1)	O(1)	144.71(6)
O(5)	Er(1)	O(3)	84.77(6)
O(5)	Er(1)	N(1)	139.21(6)
O(5)	Er(1)	N(4)	73.04(6)
O(5)	Er(1)	N(7)	65.06(6)
O(6)	Er(1)	O(1)	76.48(6)
O(6)	Er(1)	O(2)	83.40(6)
O(6)	Er(1)	O(3)	83.51(6)
O(6)	Er(1)	O(4)	142.72(6)
O(6)	Er(1)	O(5)	130.25(6)
O(6)	Er(1)	N(1)	69.69(6)
O(6)	Er(1)	N(4)	139.06(7)
O(6)	Er(1)	N(7)	65.20(6)
N(1)	Er(1)	N(7)	118.84(6)
N(4)	Er(1)	N(1)	117.38(6)
N(4)	Er(1)	N(7)	123.78(6)

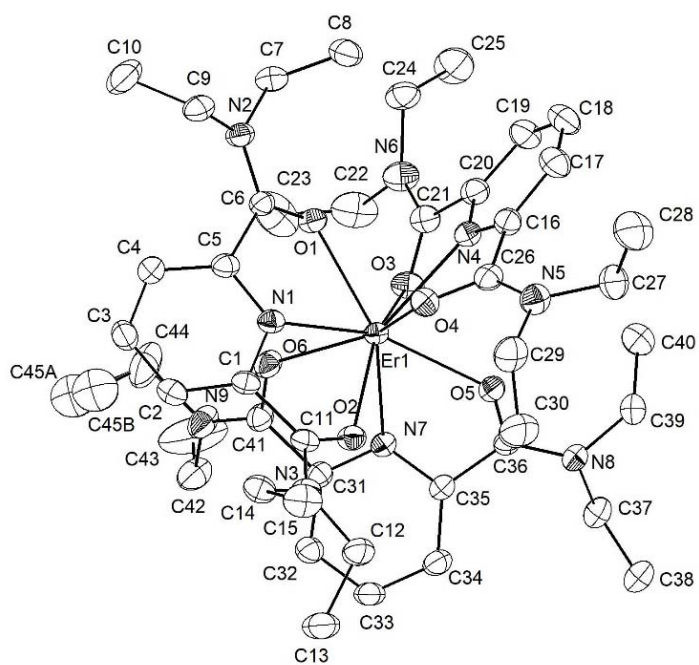
Table S7. Selected least-squares planes data for complex $[\text{Er}(\text{dpa-amide})_3](\text{ClO}_4)_3$ (**3**).

Least-squares planes

Least-squares planes description	Abbreviation	Max. deviation/ \AA	Atom
Pyridine 1 N(1) C(1) C(2) C(3) C(4) C(5)	Py1	0.024	N(1)
Pyridine 2 N(4) C(16) C(17) C(18) C(19) C(20)	Py2	0.028	C(16)
Pyridine 3 N(7) C(31) C(32) C(33) C(34) C(35)	Py3	0.033	N(7)

Interplanar angles ($^{\circ}$)

	Py1	Py2	Py3
Py1		67.07(9)	29.51(8)
Py2			61.66(9)
Py3			

**Figure S4.** ORTEP molecular view with numbering scheme of the asymmetric unit for $[\text{Er}(\text{dpa-amide})_3]^{3+}$ in the crystal structure of $[\text{Er}(\text{dpa-amide})_3](\text{ClO}_4)_3$ (**3**). Thermal ellipsoids are represented at 50% probability level and hydrogen atoms are omitted for clarity.

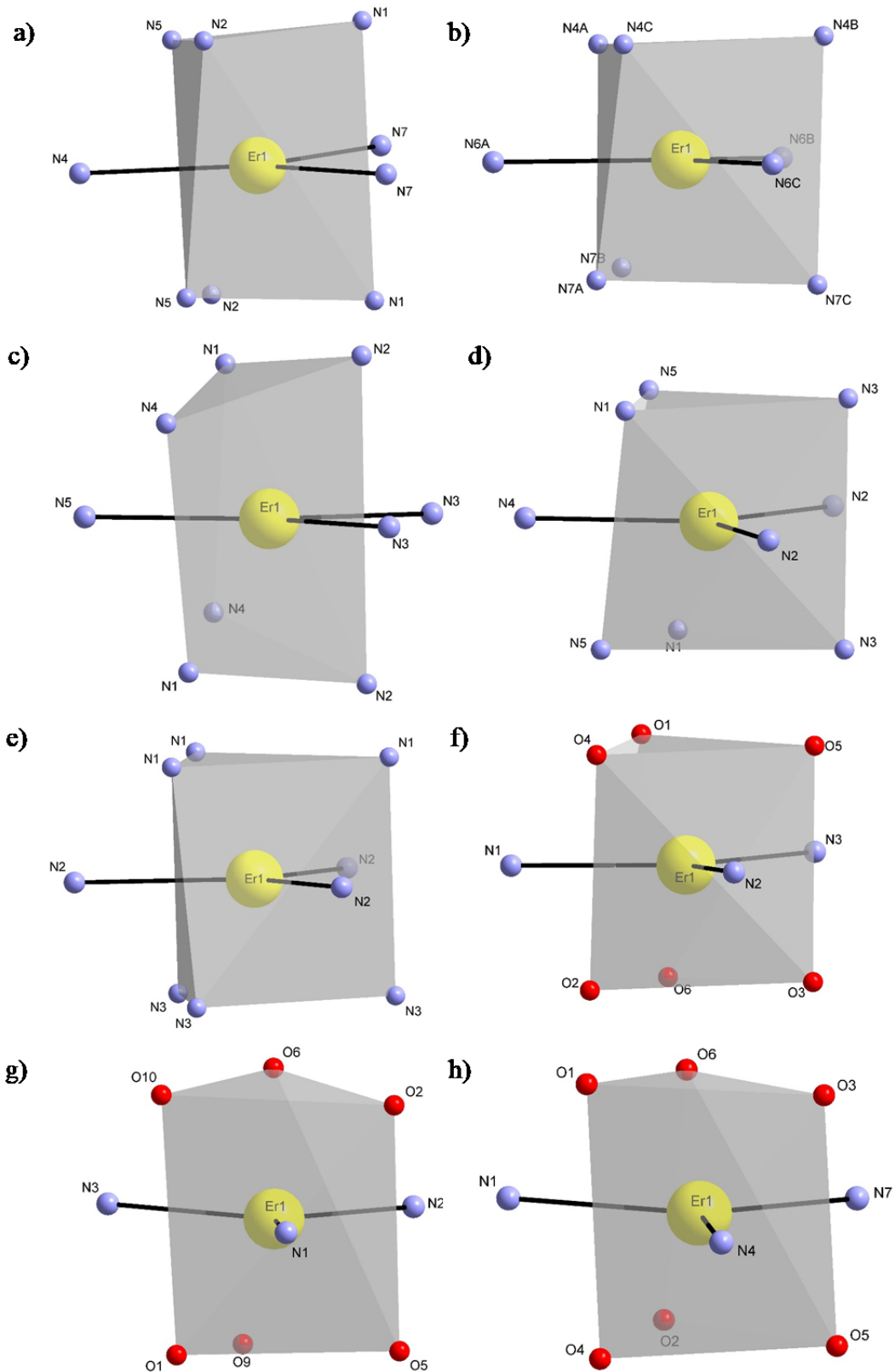


Figure S5. Schematic representations of the polyhedra formed around Er(III) in the solid state for a) $[\text{Er}(\text{Et-bzmpy})_3]^{3+}$, b) $[\text{GaErGa}(\text{bpb-bzimpy})_3]^{9+}$, c) $[\text{Er}(\text{tpy})_3]^{3+}$, d) $[\text{Er}(\text{Me-tpy})_3]^{3+}$, e) $[\text{Er}(\text{Et-tpy})_3]^{3+}$, f) $[\text{Er}(\text{dpa})_3]^{3-}$, g) $[\text{Er}(\text{dpa-ester})_3]^{3+}$ and h) $[\text{Er}(\text{dpa-amide})_3]^{3+}$.

Table S8. Structural data of complexes $(\text{NHEt}_3)_5[\text{Er}(\text{dpa})_3](\text{CF}_3\text{SO}_3)_2$ (**1**), $[\text{Er}(\text{dpa-ester})_3](\text{ClO}_4)_3$ (**2**), $[\text{Er}(\text{dpa-diamide})_3](\text{ClO}_4)_3$ (**3**), $[\text{Er}(\text{Et-bzimpy})_3](\text{ClO}_4)_3 \cdot 2\text{CH}_3\text{CN}$,²⁸ $[\text{Er}(\text{tpy})_3](\text{ClO}_4)_3$,²⁸ $[\text{Er}(\text{Et-tpy})_3](\text{ClO}_4)_3 \cdot 1.5\text{CH}_3\text{CN}$ ²⁸ and $[\text{GaErGa}(\text{bpbbzimpy})_3]_2(\text{CF}_3\text{SO}_3)_{18} \cdot 30\text{C}_3\text{H}_5\text{N}$ ¹² in the solid state.

Complexes	Er(III) entity	$\delta_{\text{Ln},\text{N(all)}} / \text{\AA}^a$	$\delta_{\text{Ln},\text{N(Py)}} / \text{\AA}^b$	$\delta_{\text{Ln},\text{O}} / \text{\AA}$	$D_{3\text{h}}^c$
$[\text{Er}(\text{dpa})_3](\text{CF}_3\text{SO}_3)_2(\text{HNEt}_3)_5$	N_3O_6	-	2.47(2)	2.38(3)	1.592
$[\text{Er}(\text{dpa-ester})_3](\text{ClO}_4)_3$	N_3O_6	-	2.446(2)	2.39(1)	2.678
$[\text{Er}(\text{dpa-amide})_3](\text{ClO}_4)_3$	N_3O_6	-	2.50(2)	2.35(2)	1.544
$[\text{Er}(\text{tpy})_3](\text{ClO}_4)_3$	N_9	2.52(3)	2.50(3)	-	2.119
$[\text{Er}(\text{Et-tpy})_3](\text{ClO}_4)_3$	N_9	2.52(2)	2.51(3)	-	2.175
$[\text{Er}(\text{Et-bzimpy})_3](\text{ClO}_4)_3$	N_9	2.52(5)	2.49(1)	-	3.296
$[\text{GaErGa}(\text{bpbbzimpy})_3]_2(\text{CF}_3\text{SO}_3)_9^{[d]}$	N_9	2.52(2)	2.52(2)	-	1.991

^a Average bond distances $\delta_{\text{Ln},\text{N}}$ for all nitrogen donor atoms of the ligands. ^b Average bond distances $\delta_{\text{Ln},\text{N}}$ for the nitrogen donor atoms of the central pyridine rings in the ligands. ^c SHAPE's³⁴ scores as compared to an ideal tricapped trigonal prism geometry ($D_{3\text{h}}$). ^d Average value for two complexes in the asymmetric unit.

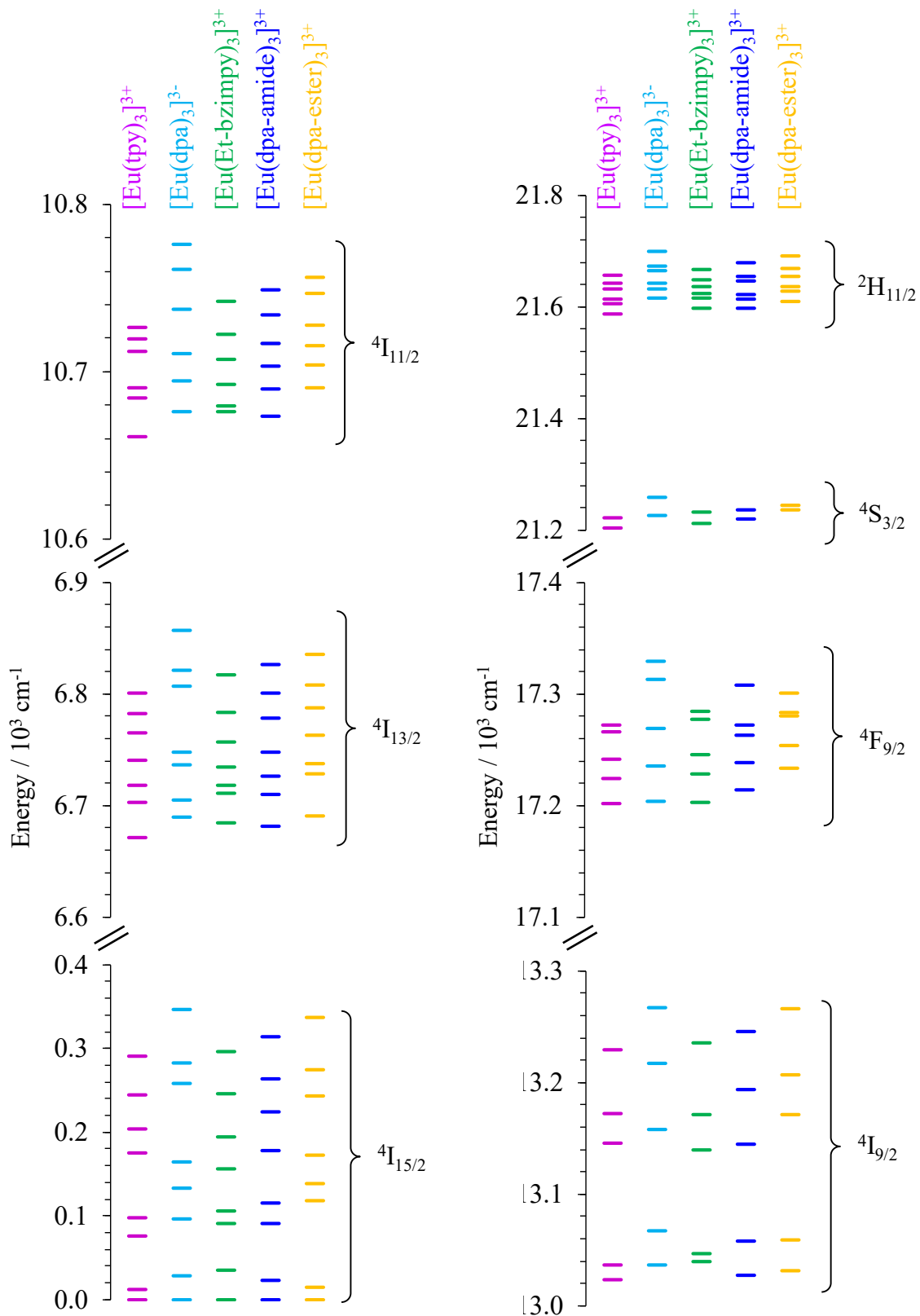


Figure S6. Energy levels issued from selected $^{2S+1}L_J$ terms calculated by SO-CASSCF(PT2shift) for $[\text{Er(tpy)}_3](\text{ClO}_4)_3$,²⁸ $[\text{Er(Et-bzimpy)}_3](\text{ClO}_4)_3 \cdot 2\text{CH}_3\text{CN}$,²⁸ $(\text{NHEt}_3)_5[\text{Er(dpa)}_3](\text{CF}_3\text{SO}_3)_2$ (**1**), $[\text{Er(dpa-amide)}_3](\text{ClO}_4)_3$ (**2**) and $[\text{Er(dpa-ester)}_3](\text{ClO}_4)_3$ (**3**) complexes

Table S9. Crystal-field (\bar{B}_q^k)^a and Strength (S^k , S_q and S)^b parameters (cm^{-1}) computed using the SO-CASSCF(PT2shift) approach for the crystal structures of $[\text{Er(tpy)}_3](\text{ClO}_4)_3$, $[\text{Er(Et-bzimpy)}_3](\text{ClO}_4)_3 \cdot 2\text{CH}_3\text{CN}$, $(\text{NHEt}_3)_5[\text{Er(dpa)}_3](\text{CF}_3\text{SO}_3)_2$ (**1**), $[\text{Er(dpa-amide)}_3](\text{ClO}_4)_3$ (**2**), $[\text{Er(dpa-ester)}_3](\text{ClO}_4)_3$ (**3**).

	Er(tpy) ₃	Er(Et-bzimpy) ₃	Er(dpa) ₃ -A	Er(dpa) ₃ -B	Er(dpa-amide) ₃	Er(dpa-ester) ₃
\bar{B}_0^2	-238	-30	417	358	32	59
\bar{B}_1^2	52	47	51	14	107	57
\bar{B}_2^2	23	221	206	122	140	37
\bar{B}_0^4	-237	-177	-387	-342	-422	-283
\bar{B}_1^4	85	9	46	72	50	30
\bar{B}_2^4	6	82	14	30	24	31
\bar{B}_3^4	151	120	371	344	313.	272.
\bar{B}_4^4	20	149	113	69	85	107
\bar{B}_0^6	-269	-247	-356	-341	-246	-429
\bar{B}_1^6	20	50	39	24	39	37
\bar{B}_2^6	33	164	132	89	68	94
\bar{B}_3^6	226	166	295	289	268	311
\bar{B}_4^6	9	96	128	91	51	80
\bar{B}_5^6	15	91	131	67	64	83
\bar{B}_6^6	461	398	368	433	438	402

S	155	157	228	206	186	171
S^2	112	144	230	178	112	50
S^4	114	115	225	204	209	168
S^6	215	201	228	232	217	240
S_0	152	91	247	218	157	154
S_1	52	36	42	36	73	41
S_2	19	159	140	86	93	46
S_3	114	86	210	197	181	177
S_4	10	80	73	48	45	59
S_5	6	35	51	26	25	32
S_6	181	156	144	170	171	157

^a The Z axis was chosen as the pseudo-threefold crystallographic axis and the choice of X and Y axes is arbitrary. Hence, only the norm of the crystal field parameters is considered with $\overline{B}_q^k = \sqrt{\left|B_q^k\right|^2 + \left|B_{-q}^k\right|^2}$. ^b For reducing the number of crystal field parameters, we considered the rotational invariant

strength parameters of k th order $S^k = \sqrt{\left(\frac{1}{2k+1}\right) \sum_{q=-k}^k \left|B_q^k\right|^2}$ and the global strength parameter $S = \sqrt{\frac{1}{3} \sum_k \left(S^k\right)^2}$. Estimates of the symmetry about the

Z axis were obtained by the strength parameters of q th index $S_q = \sqrt{\sum_k \left(\frac{1}{2k+1}\right) \left|B_q^k\right|^2}$, which is invariant to rotations about the Z axis.³⁷ Altogether $S = \sqrt{(S^2 + S^4 + S^6)/3} = \sqrt{(S_0 + S_1 + S_2 + S_3 + S_4 + S_5 + S_6)/3}$.

Table S10. Energies of the Kramers doublets issued from the Er($^4I_{15/2}$) ground term (ΔE /cm $^{-1}$), associated g-factors and decomposition in terms of M_J components with Z axis as the pseudo-threefold crystallographic axis computed using SO-CASSCF(PT2shift) method for the crystal structure of [Er(tpy)₃](ClO₄)₃.

	ΔE	g_i	composition M_J
1-2	0	10.8;4.9;1.8	43% $\pm 15/2$; 30% $\pm 9/2$
3-4	12	11.0;4.1;2.2	47% $\pm 7/2$; 35% $\pm 5/2$
5-6	76	11.4;1.0;0.1	23% $\pm 1/2$; 21% $\pm 15/2$; 21% $\pm 11/2$
7-8	98	7.3;6.4;2.5	25% $\pm 1/2$; 22% $\pm 15/2$; 19% $\pm 11/2$; 18% $\pm 3/2$
9-10	175	7.2;2.1;1.2	61% $\pm 13/2$; 23% $\pm 5/2$
11-12	204	5.3;3.1;2.5	34% $\pm 11/2$; 24% $\pm 7/2$; 22% $\pm 5/2$; 15% $\pm 1/2$
13-14	245	3.8;3.4;1.0	49% $\pm 3/2$; 42% $\pm 9/2$
15-16	291	10.5;5.5;1.9	35% $\pm 1/2$; 19% $\pm 13/2$; 16% $\pm 7/2$; 15% $\pm 11/2$

Table S11. Energies of the Kramers doublets issued from the Er($^4I_{15/2}$) ground term (ΔE /cm $^{-1}$), associated g-factors and decomposition in terms of M_J components with Z axis as the pseudo-threefold crystallographic axis computed using SO-CASSCF(PT2shift) method for the crystal structure of [Er(Et-bzimpy)₃](ClO₄)₃.2CH₃CN.

	ΔE	g_i	composition M_J
1-2	0	13.7; 1.8; 1.1	37% 7/2; 28% 5/2; 16% 9/2
3-4	35	10.2; 4.2; 4.0	26% 9/2; 25% 15/2; 14% 7/2; 14% 3/2
5-6	90	10.6; 3.2; 2.0	25% 1/2; 22% 3/2; 17% 11/2; 13% 15/2
7-8	106	8.6; 3.5; 0.5	40% 15/2; 25% 1/2; 11% 3/2
9-10	157	10.6; 3.3; 1.7	27% 5/2; 25% 7/2; 12% 11/2
11-12	194	5.5; 4.7; 2.2	50% 13/2; 26% 11/2
13-14	246	10.5; 1.8; 0.1	26% 1/2; 23% 9/2; 15% 3/2; 14% 11/2; 13% 13/2
15-16	291	13.0; 3.0; 2.5	19% 7/2; 17% 5/2; 14% 1/2; 14% 3/2; 14% 11/2; 13% 13/2

Table S12. Energies of the Kramers doublets issued from the Er($^4I_{15/2}$) ground term (ΔE /cm $^{-1}$), associated *g*-factors and decomposition in terms of M_J components with *Z* axis as the pseudo-threefold crystallographic axis computed using SO-CASSCF(PT2shift) method for the crystal structure of (NHEt₃)₅[Er(dpa)₃](CF₃SO₃)₂.

A				B			
	ΔE	g_i	composition M_J		ΔE	g_i	composition M_J
1-2	0	12.4;3.6;2.1	46% $\pm 7/2$; 34% $\pm 5/2$	0	12.1;4.2;2.0	48% $\pm 7/2$; 39% $\pm 5/2$	
3-4	27	9.4;3.8;2.7	37% $\pm 9/2$; 22% $\pm 3/2$; 24% $\pm 15/2$	25	8.9;3.7;2.3	41% $\pm 9/2$; 26% $\pm 3/2$; 23% $\pm 15/2$	
5-6	96	14.3;1.6;0.0	41% $\pm 1/2$; 22% $\pm 11/2$; 16% $\pm 5/2$	105	10.7;5.3;1.1	63% $\pm 1/2$; 17% $\pm 11/2$	
7-8	133	8.7;2.0;0.1	30% $\pm 1/2$; 19% $\pm 15/2$; 22% $\pm 3/2$	134	5.1;4.0;1.5	37% $\pm 15/2$; 32% $\pm 3/2$	
9-10	164	8.5;3.5;0.4	20% $\pm 5/2$; 25% $\pm 7/2$; 20 $\pm 15/2$	177	8.2;5.6;0.7	32% $\pm 5/2$; 28% $\pm 7/2$	
11-12	258	6.8;4.3;1.7	30% $\pm 11/2$; 19% $\pm 13/2$; 21% $\pm 9/2$	259	5.1;4.2;3.0	39% $\pm 11/2$; 26% $\pm 13/2$	
13-14	283	11.7;2.8;0.0	24% $\pm 9/2$; 30% $\pm 11/2$; 13% $\pm 15/2$	278	11.0;1.2;0.1	33% $\pm 9/2$; 19% $\pm 11/2$; 17% $\pm 15/2$	
15-16	346	10.7;5.9;3.0	54% $\pm 13/2$; 15% $\pm 7/2$	340	8.2;6.9;4.9	51% $\pm 13/2$; 15% $\pm 7/2$	

Table S13. Energies of the Kramers doublets issued from the Er($^4I_{15/2}$) ground term (ΔE /cm $^{-1}$), associated *g*-factors and decomposition in terms of M_J components with *Z* axis as the pseudo-threefold crystallographic axis computed using SO-CASSCF method for the crystal structure of [Er(dpa-amide)₃](ClO₄)₃ (**2**).

	ΔE	g_i	composition M_J
1-2	0	11.2; 5.1; 2.9	25% $7/2$; 21% $9/2$; 20% $5/2$; 19% $15/2$
3-4	23	9.8; 4.5; 0.6	25% $15/2$; 23% $7/2$; 21% $5/2$; 16% $9/2$
5-6	91	9.0; 5.1; 1.8	57% $1/2$; 22% $11/2$
7-8	115	6.8; 3.1; 0.7	40% $3/2$; 36% $15/2$
9-10	178	8.7; 5.1; 2.1	38% $5/2$; 21% $7/2$; 20% $13/2$
11-12	225	5.4; 4.5; 0.5	65% $11/2$
13-14	264	9.0; 1.8; 0.4	41% $9/2$; 26% $3/2$
15-16	314	10.5; 5.4; 3.2	29% $13/2$; 20% $7/2$; 13% $11/2$

Table S14. Energies of the Kramers doublets issued from the Er($^4I_{15/2}$) ground term (ΔE /cm $^{-1}$), associated *g*-factors and decomposition in terms of M_J components computed using SO-CASSCF(PT2shift) method for the crystal structure of [Er(dpa-ester)₃](ClO₄)₃ (**3**).

	ΔE	g_i	composition M_J
1-2	0	2.4;5.6;10.2	32% $7/2$; 23 % $15/2$; 19% $5/2$; 18% $9/2$
3-4	14	2.7;3.8;10.5	25% $9/2$; 24% $7/2$; 20% $15/2$; 19% $5/2$
5-6	118	1.6;3.6;8.1	33% $3/2$; 25% $15/2$; 17% $1/2$; 11% $11/2$
7-8	137	1.8;4.0;9.0	43% $1/2$; 17% $11/2$; 15% $15/2$; 11% $3/2$
9-10	172	0.1;4.4;10.2	39% $5/2$; 26% $7/2$; 12% $13/2$; 12% $11/2$
11-12	243	0.5;4.1;5.1	27% $11/2$; 26% $13/2$; 17% $9/2$; 14% $3/2$
13-14	274	0.6;2.1;9.5	26% $9/2$; 21% $3/2$; 22% $11/2$; 11% $13/2$
15-16	336	5.7;6.7;7.4	44% $13/2$; 23% $1/2$; 14% $7/2$ 10% $11/2$

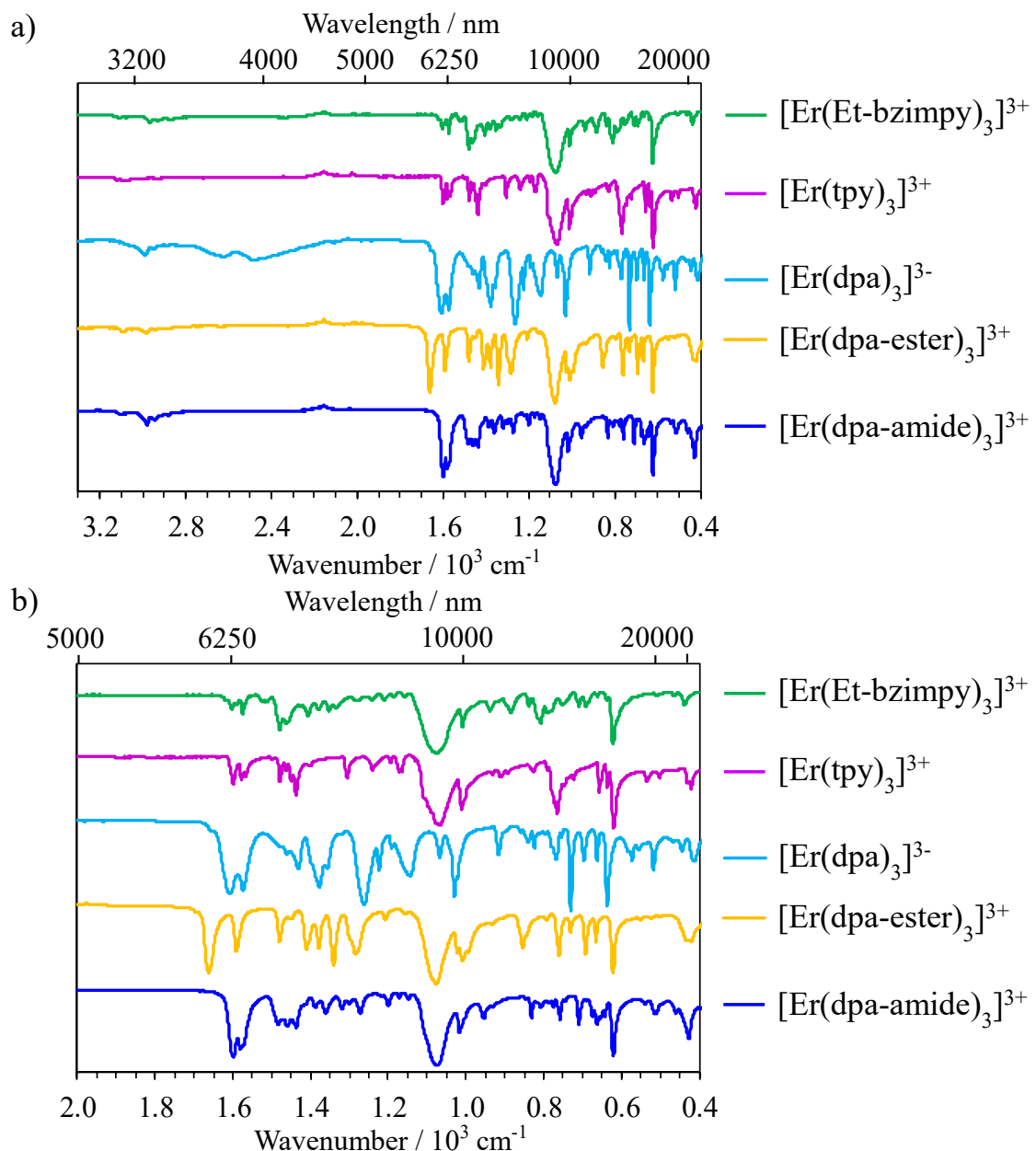


Figure S7. Infrared vibrational spectra recorded for crystals of $[\text{Er}(\text{tpy})_3](\text{ClO}_4)_3$,²⁸ $[\text{Er}(\text{Et-bzimpy})_3](\text{ClO}_4)_3 \cdot 2\text{CH}_3\text{CN}$,²⁸ $(\text{NHEt}_3)_5[\text{Er}(\text{dpa})_3](\text{CF}_3\text{SO}_3)_2$ (**1**), $[\text{Er}(\text{dpa-amide})_3](\text{ClO}_4)_3$ (**2**), $[\text{Er}(\text{dpa-ester})_3](\text{ClO}_4)_3$ (**3**).

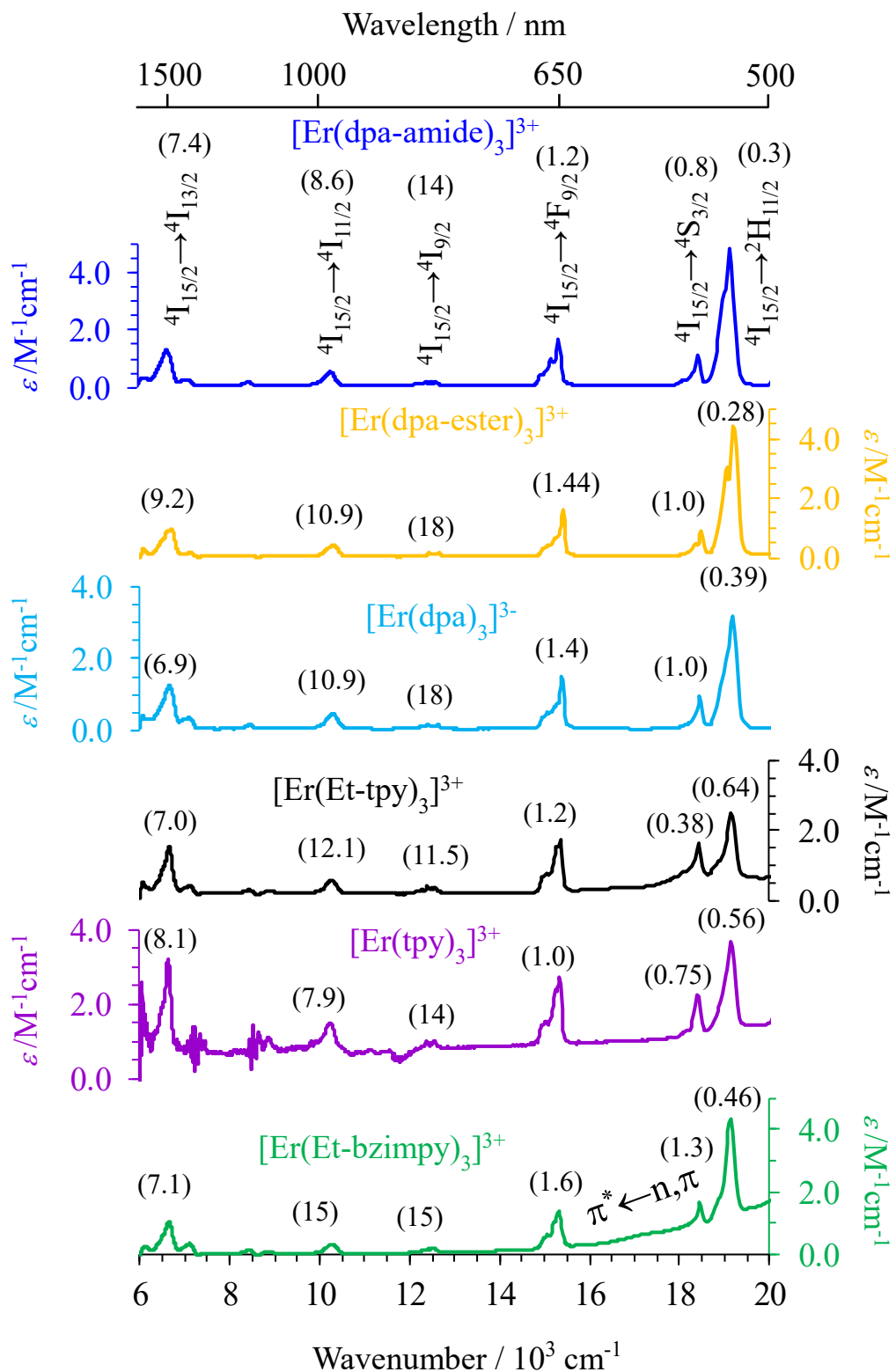


Figure S8 NIR-VIS absorption spectra of $[Er(L)_3]^{3+}$ ($L = Et\text{-bzimpy}$, Et-tpy, tpy dpa-amide, dpa-ester) and $[Er(dpa)_3]^{3-}$ (3 mM in acetonitrile at 298 K) showing the $Er(^{2S+1}L_J \leftarrow ^4I_{15/2})$ transitions and the associated radiative lifetimes (Eqs 2-3 in ms) between parenthesis.

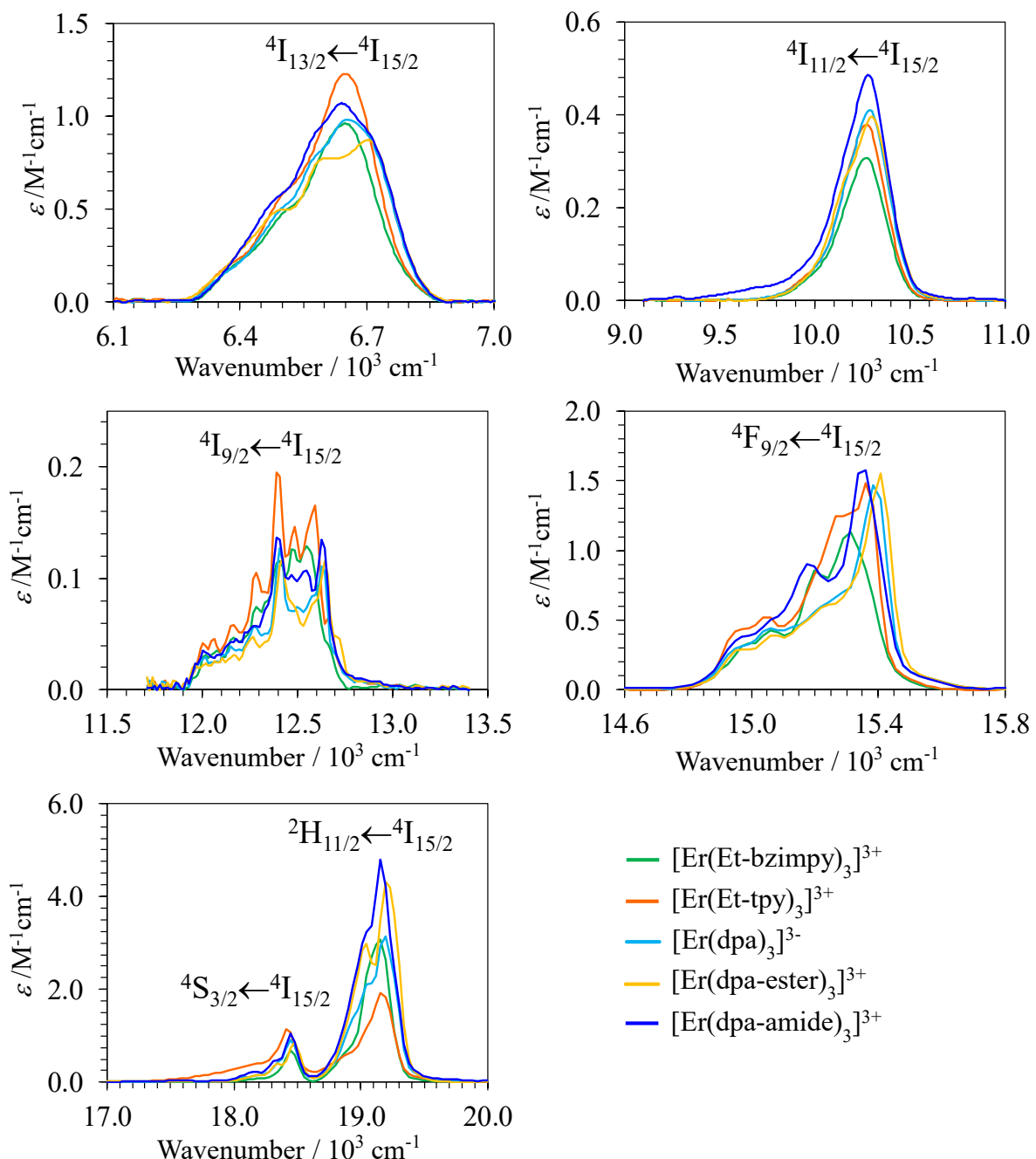


Figure S9 Enlargement of each $\text{Er}({}^{2S+1}\text{L}_J \leftarrow {}^4\text{I}_{15/2})$ transition in the NIR-VIS absorption spectra of $[\text{Er}(\mathbf{L})_3]^{3+}$ (\mathbf{L} = Et-bzimpy, Et-tpy, tpy dpa-amide, dpa-ester) and $[\text{Er}(\text{dpa})_3]^{3-}$ (3 mM in acetonitrile at 298 K).

Table S15. Radiative lifetimes calculated using $\frac{1}{\tau_{\text{rad}}} = 2303 \cdot \frac{8\pi cn^2 \tilde{\nu}_m^2 (2J+1)}{N_A (2J'+1)} \int \varepsilon(\tilde{\nu}) d\tilde{\nu}$ (Eqs 2-3) for selected Er(III) excited levels in [GaErGa(bpbbzimpy)₃]⁹⁺, [Er(L)₃]³⁺ (L = Et-bzimpy, Et-tpy, tpy dpa-amide, dpa-ester) and [Er(dpa)₃]³⁻ in acetonitrile (3mM) at 298 K.

Compound	$\tau_{\text{Er,rad}}^{4\text{I}_{13/2}}$	$\tau_{\text{Er,rad}}^{4\text{I}_{11/2}}$	$\tau_{\text{Er,rad}}^{2\text{I}_{9/2}}$	$\tau_{\text{Er,rad}}^{4\text{F}_{9/2}}$	$\tau_{\text{Er,rad}}^{4\text{S}_{3/2}}$	$\tau_{\text{Er,rad}}^{2\text{H}_{11/2}}$	$\tau_{\text{Er,rad}}^{4\text{F}_{7/2}}$	$\tau_{\text{Er,rad}}^{4\text{F}_{5/2}}$	$\tau_{\text{Er,rad}}^{4\text{F}_{3/2}}$	$\tau_{\text{Er,rad}}^{2\text{G}_{9/2}}$	$\tau_{\text{Er,rad}}^{4\text{G}_{11/2}}$	$\tau_{\text{Er,rad}}^{4\text{G}_{9/2}}$
	ms	ms	ms	ms	ms	ms	ms	ms	ms	ms	ms	ms
[Er(Et-bzimpy) ₃] ³⁺	7.12(5)	15(1)	15(1)	1.6(1)	1.31(9)	0.46(3)	0.82(6)	^a	^a	^a	^a	^a
GaErGa(bpbbzimpy) ₃] ⁹⁺	9.4(5)	12.9(6)	25(1)	1.5(1)	1.6(1)	0.64(3)	^a	^a	^a	^a	^a	^a
[Er(tpy) ₃] ³⁺	8.1(6)	7.9(6)	14(1)	0.99(7)	0.75(5)	0.56(4)	0.52(4)	0.92(6)	0.91(6)	^a	^a	^a
[Er(Et-tpy) ₃] ³¹	7.01(5)	12.1(8)	11.5(8)	1.23(9)	0.38(3)	0.64(4)	0.59(4)	1.22(9)	1.28(9)	^a	^a	^a
[Er(dpa) ₃] ³⁻	6.9(5)	10.9(8)	18(1)	1.4(1)	0.98(7)	0.39(3)	0.58(4)	0.88(6)	0.87(6)	1.1(1)	0.11(1)	1.12(8)
[Er(dpa-ester) ₃] ³⁺	9.2(6)	10.9(8)	18(1)	1.44(1)	1.01(5)	0.28(2)	0.58(4)	0.95(7)	0.93(6)	1.27(9)	0.08(1)	1.19(8)
[Er(dpa-amide) ₃] ³⁺	7.4(5)	8.6(6)	14(1)	1.2(1)	0.81(6)	0.28(2)	0.46(3)	0.70(5)	0.77(5)	0.92(6)	0.07(1)	0.71(5)

^a Masked by intense ligand-centered absorption

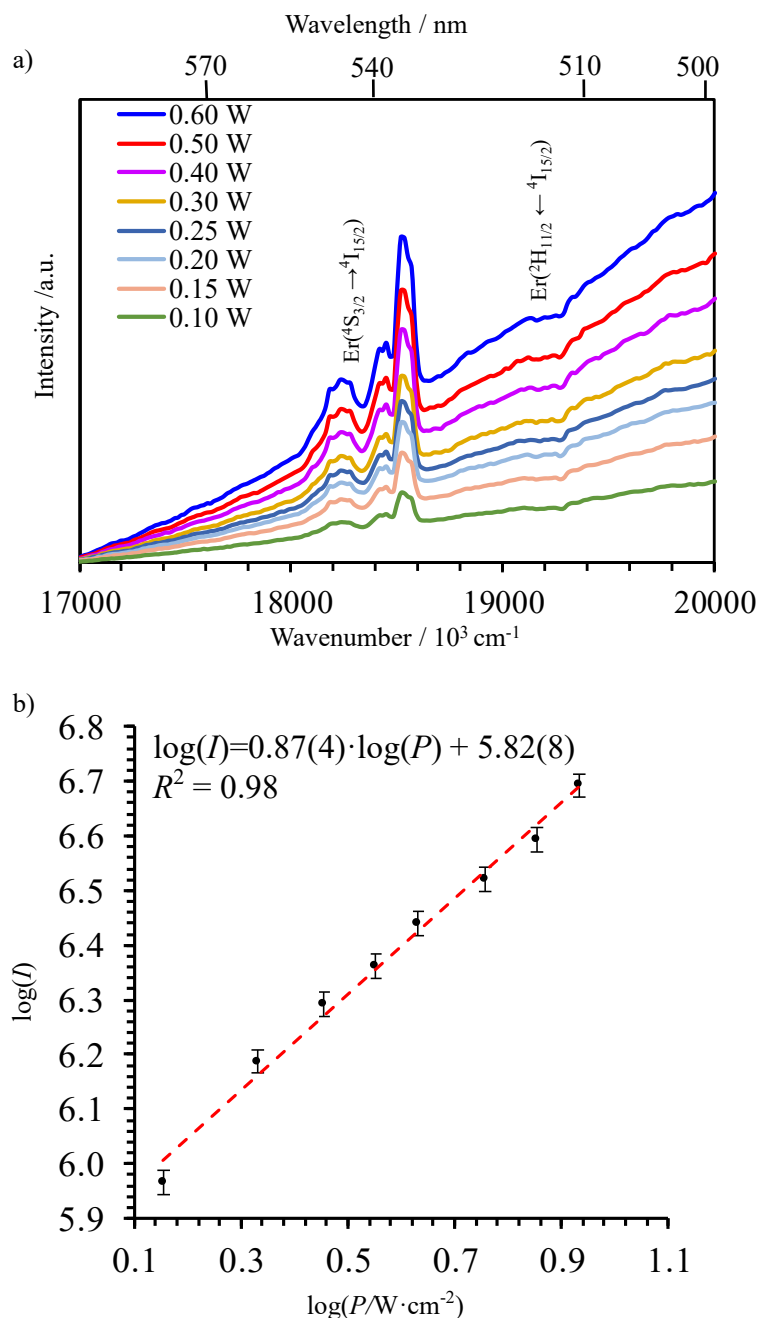


Figure S10 a) Solid state visible part of the luminescence spectra of $[\text{GaErGa(bpbzimpy)}_3](\text{CF}_3\text{SO}_3)_9$ at 298 K ($\lambda_{\text{exc}} = 400 \text{ nm}$, $\tilde{\nu}_{\text{exc}} = 25000 \text{ cm}^{-1}$) and b) corresponding log-log plot of intensities I as a function of incident pump intensities P (in $\text{W} \cdot \text{cm}^{-2}$).

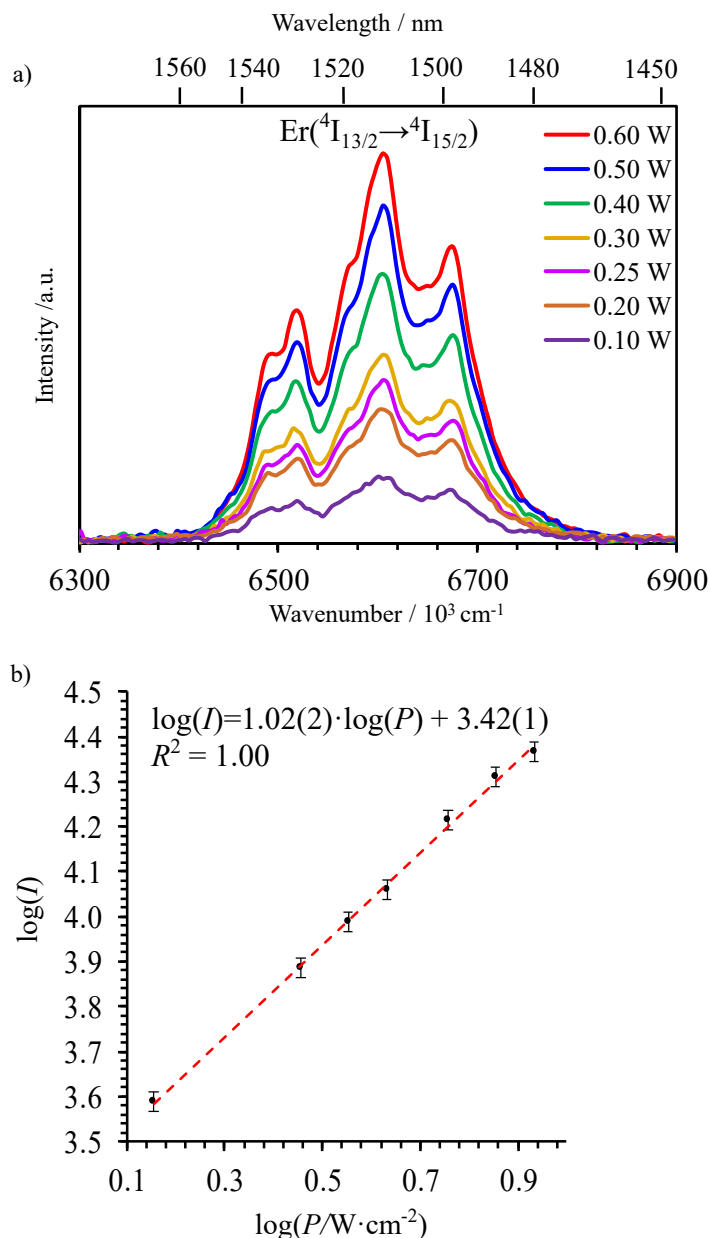


Figure S11 a) Solid state near-infrared part of the luminescence spectra of [GaErGa(bpb-bzimpy)₃](CF₃SO₃)₉ at 298 K ($\lambda_{\text{exc}} = 400 \text{ nm}$, $\tilde{\nu}_{\text{exc}} = 25000 \text{ cm}^{-1}$) and b) corresponding log-log plot of intensities I as a function of incident pump intensities P (in $\text{W} \cdot \text{cm}^{-2}$).

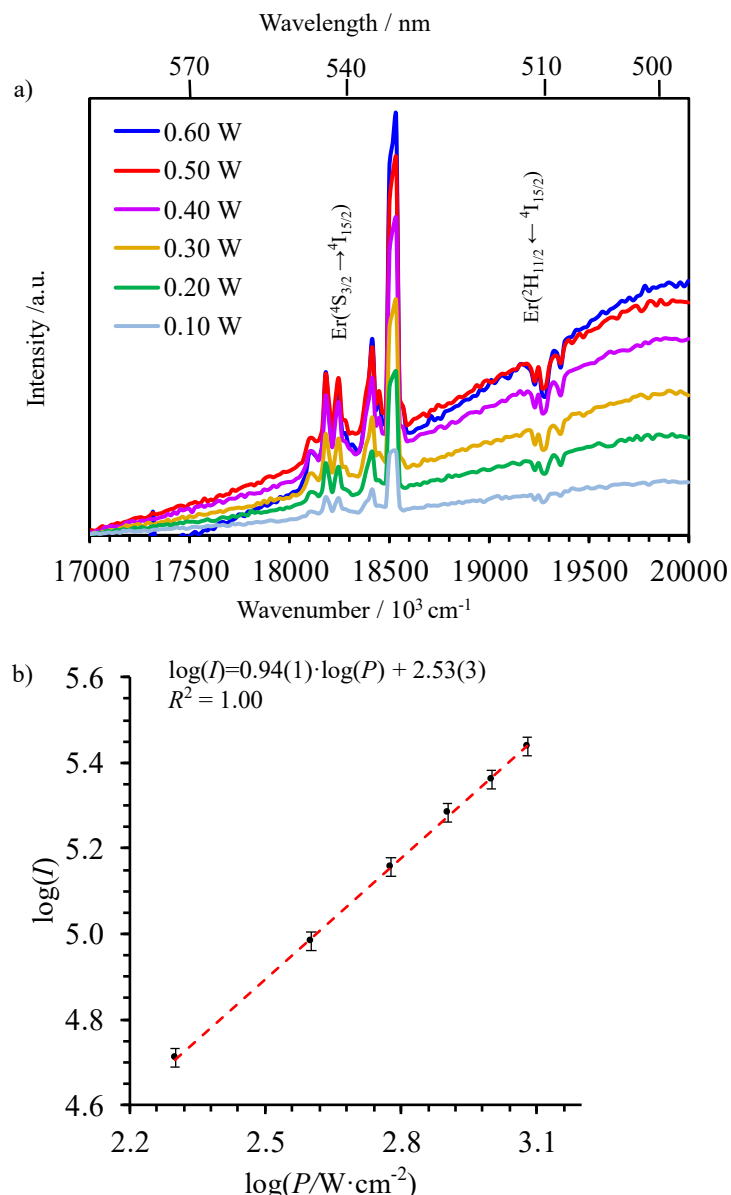


Figure S12 a) Solid state visible part of the luminescence spectra of [GaErGa(bpb-bzimpy)₃](CF₃SO₃)₉ at 10 K ($\lambda_{\text{exc}} = 400 \text{ nm}$, $\tilde{\nu}_{\text{exc}} = 25000 \text{ cm}^{-1}$) and b) corresponding log-log plot of intensities I as a function of incident pump intensities P (in $\text{W} \cdot \text{cm}^{-2}$).

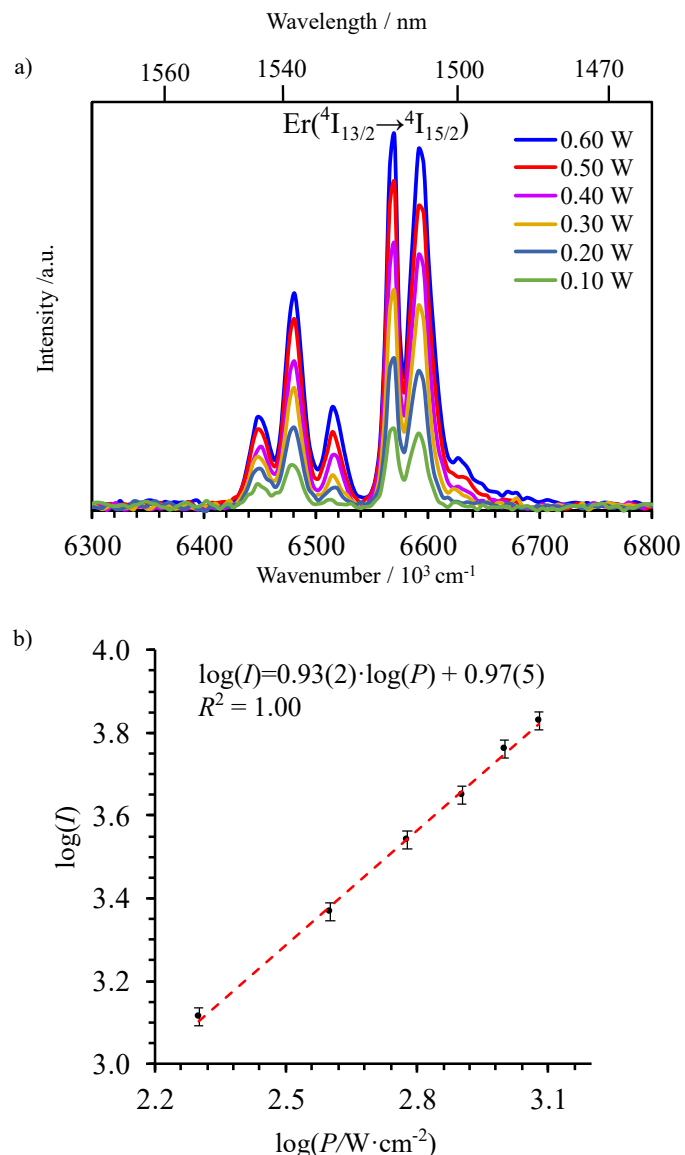


Figure S13 a) Solid state near-infrared part of the luminescence spectra of $[\text{GaErGa}(\text{bpb-bzimpy})_3](\text{CF}_3\text{SO}_3)_9$ at 10 K ($\lambda_{\text{exc}} = 400 \text{ nm}$, $\tilde{\nu}_{\text{exc}} = 25000 \text{ cm}^{-1}$) and b) corresponding log-log plot of intensities I as a function of incident pump intensities P (in $\text{W} \cdot \text{cm}^{-2}$).

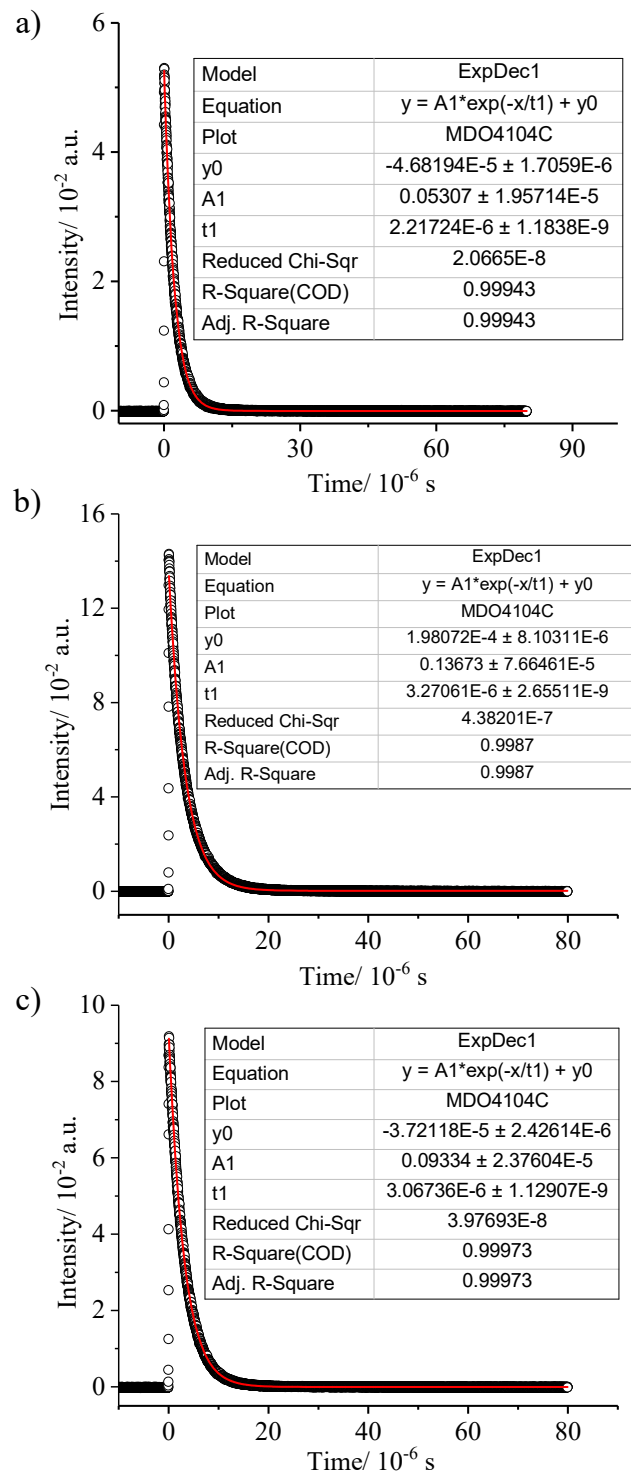


Figure S14 Decay traces of the $\text{Er}(^4\text{I}_{13/2} \rightarrow ^4\text{I}_{15/2})$ emissions observed for a) $(\text{HNEt}_3)_5[\text{Er}(\text{dpa})_3](\text{CF}_3\text{SO}_3)_2$, b) $[\text{Er}(\text{dpa-ester})_3](\text{ClO}_4)_3$ and c) $[\text{Er}(\text{dpa-amide})_3](\text{ClO}_4)_3$ in the solid state at 298 K recorded upon laser excitation of the $\text{L}(\text{L}^1\pi\pi^* \leftarrow \text{L}^1\pi\pi)$ transition at $\lambda_{\text{exc}} = 355$ nm ($\tilde{\nu}_{\text{exc}} = 28170 \text{ cm}^{-1}$).

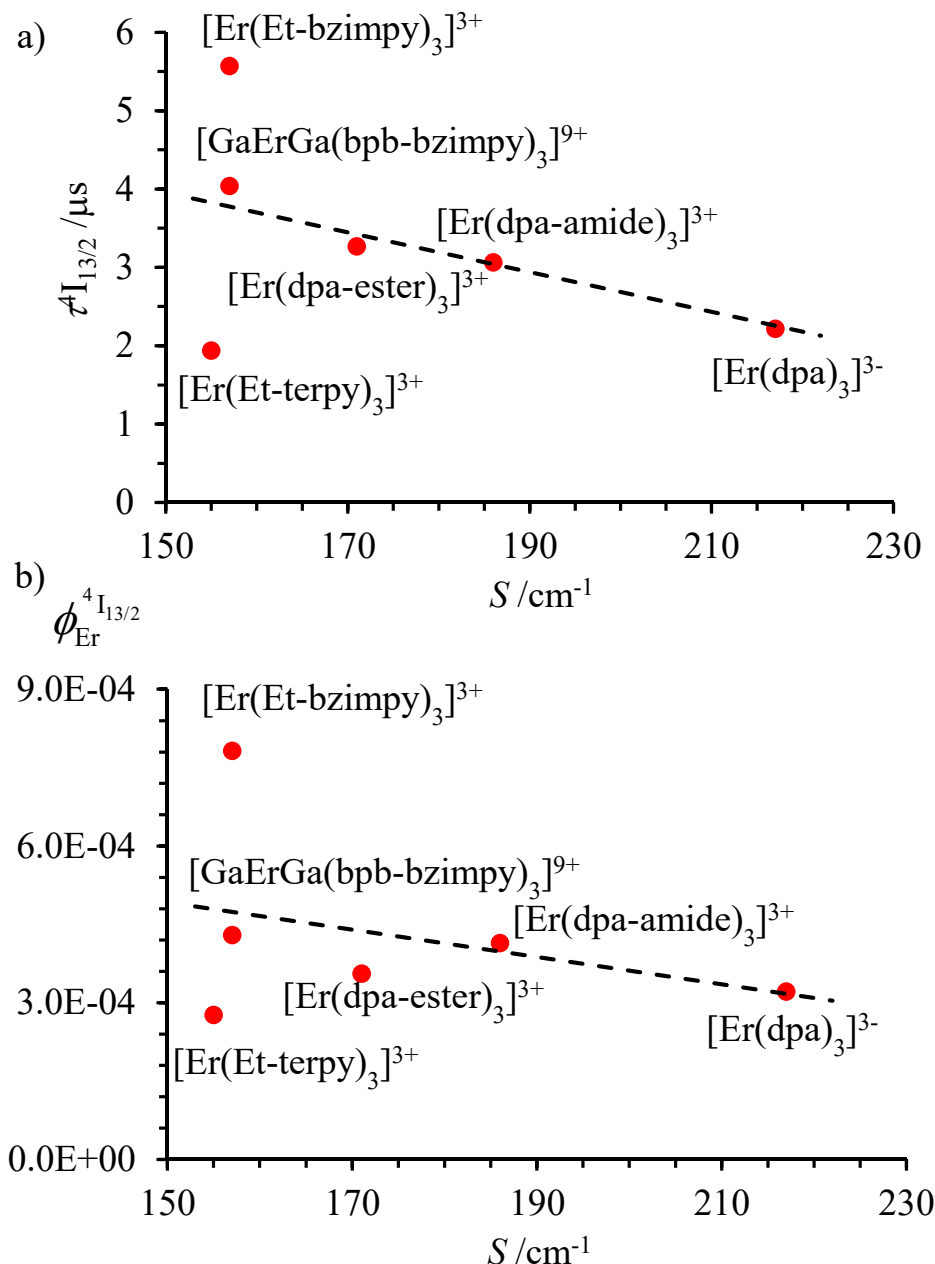


Figure S15 a) Excited lifetime of the intermediate $\text{Er}^{4\text{I}_{13/2}}$ level and b) associated intrinsic quantum yield plotted as a function of the global crystal field strengths S for $[\text{GaErGa(bpb-bzimpy)}_3]^{9+}$, $[\text{Er}(\text{L})_3]^{3+}$ ($\text{L} = \text{Et-bzimpy}, \text{Et-tpy}, \text{tpy}, \text{dpa-amide}, \text{dpa-ester}$) and $[\text{Er}(\text{dpa})_3]^{3-}$ (solid state at 298 K). The linear dashed lines are only a guide for the eyes.

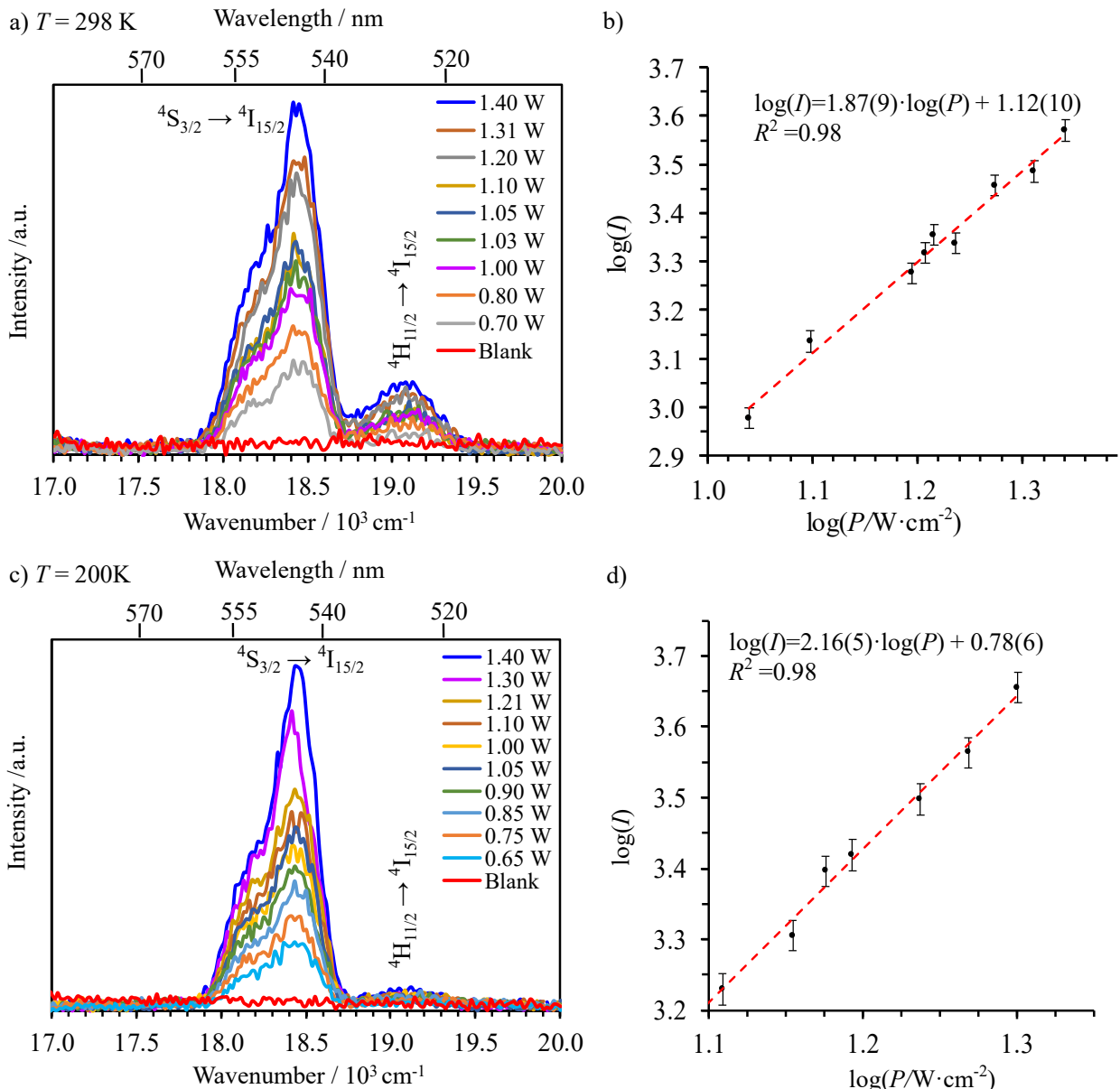


Figure S16 Upconverted visible $\text{Er}(^2\text{H}_{11/2} \rightarrow {}^4\text{I}_{15/2})$ and $\text{Er}(^4\text{S}_{3/2} \rightarrow {}^4\text{I}_{15/2})$ emissions observed for $[\text{GaErGa(bpb-bzimpy)}_3](\text{CF}_3\text{SO}_3)_9$ in the solid state at a) $T = 298 \text{ K}$ and c) $T = 200 \text{ K}$ recorded upon laser excitation of the $\text{Er}(^4\text{I}_{9/2} \leftarrow {}^4\text{I}_{15/2})$ transition at $\lambda_{\text{exc}} = 801 \text{ nm}$ ($\tilde{\nu}_{\text{exc}} = 12284 \text{ cm}^{-1}$). The blank (red curve) was recorded upon irradiation of the copper plate support covered with silver glue at maximum intensity $P = 29 \text{ W cm}^{-2}$. b) and d) corresponding log-log plot of upconverted intensities I_{up} as a function of incident pump intensities P (in $\text{W} \cdot \text{cm}^{-2}$).

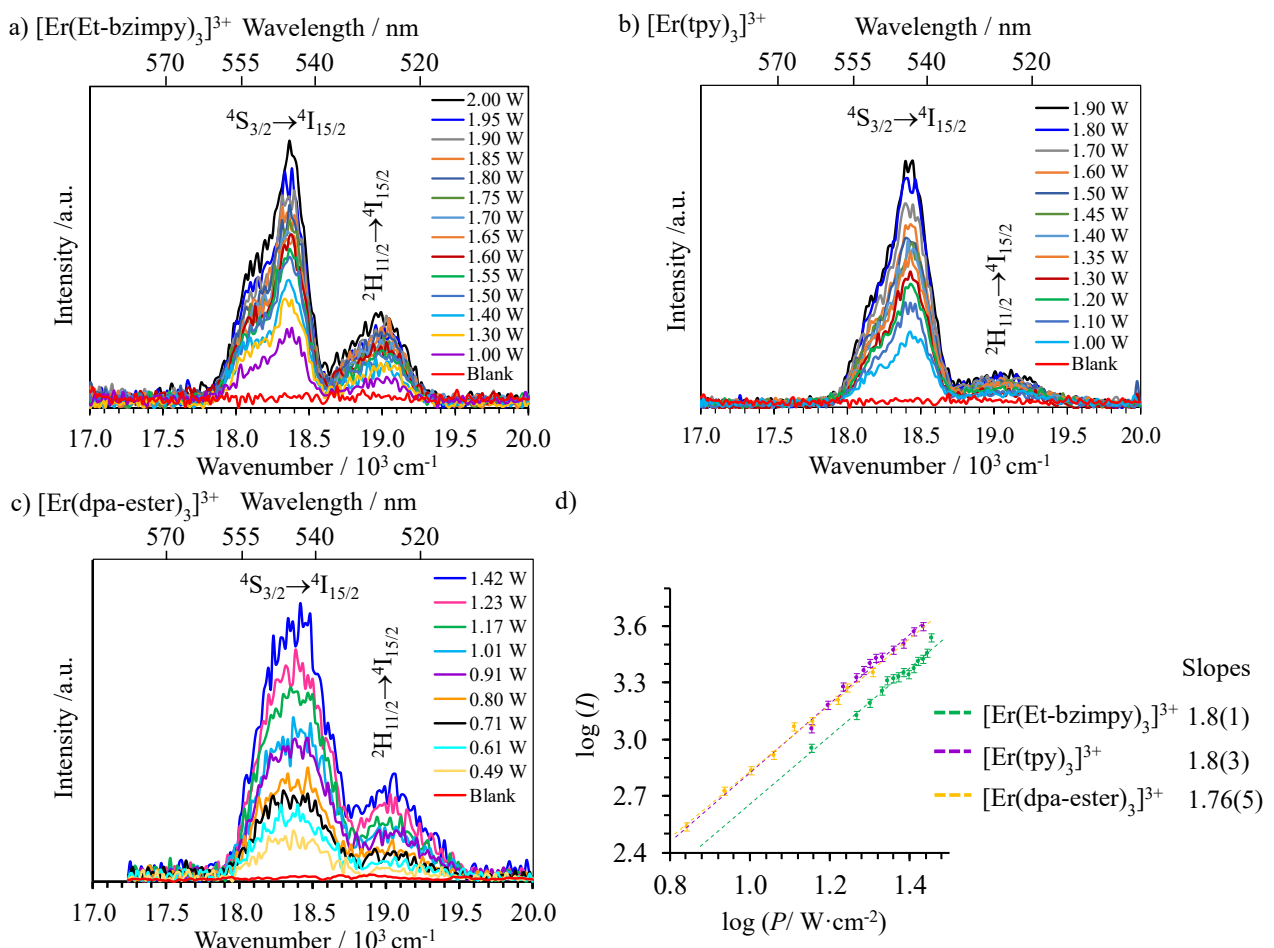


Figure S17 Upconverted visible $\text{Er}(^2\text{H}_{11/2} \rightarrow ^4\text{I}_{15/2})$ and $\text{Er}(^4\text{S}_{3/2} \rightarrow ^4\text{I}_{15/2})$ emissions observed for a) $[\text{Er}(\text{Et-bzimpy})_3](\text{ClO}_4)_3$, b) $[\text{Er}(\text{tpy})_3](\text{ClO}_4)_3$ and c) $[\text{Er}(\text{dpa-ester})_3](\text{ClO}_4)_3$ in the solid state at $T = 298$ K recorded upon laser excitation of the $\text{Er}(^4\text{I}_{9/2} \leftarrow ^4\text{I}_{15/2})$ transition at $\lambda_{\text{exc}} = 801$ nm ($\tilde{\nu}_{\text{exc}} = 12284$ cm^{-1}). The blank (red curve) was recorded upon irradiation of the copper plate support covered with silver glue at maximum intensity $P = 29$ $\text{W}\cdot\text{cm}^{-2}$. d) Corresponding log-log plot of upconverted intensities I_{up} as a function of incident pump intensities P (in $\text{W}\cdot\text{cm}^{-2}$). The upconverted signals of $(\text{HNEt}_3)_5[\text{Er}(\text{dpa})_3](\text{CF}_3\text{SO}_3)_2$ and $[\text{Er}(\text{dpa-amide})_3](\text{ClO}_4)_3$ are too weak at low intensity power to be detected at 298 K.

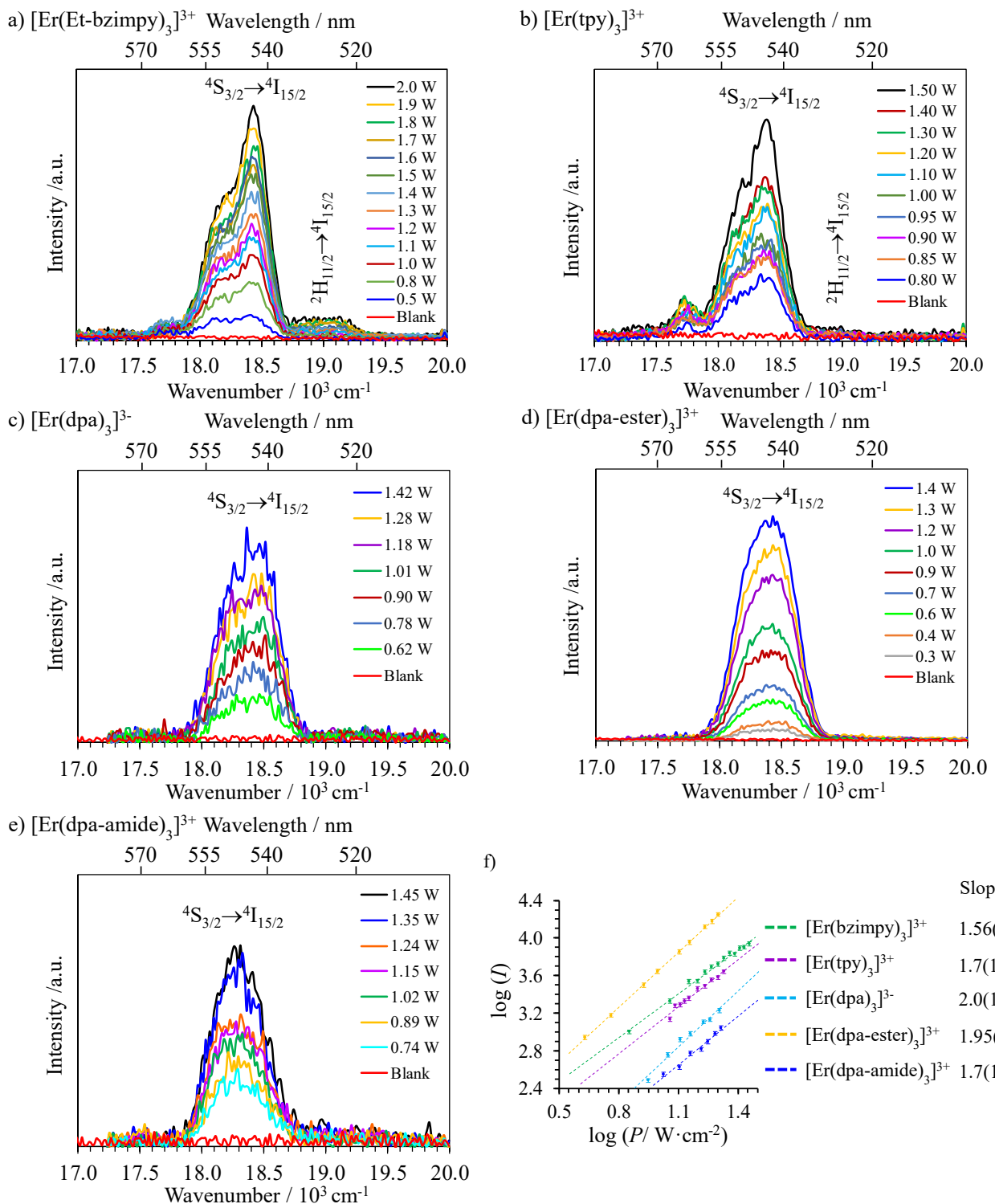


Figure S18 Upconverted visible $\text{Er}(^2\text{H}_{11/2} \rightarrow ^4\text{I}_{15/2})$ and $\text{Er}(^4\text{S}_{3/2} \rightarrow ^4\text{I}_{15/2})$ emissions observed for a) $[\text{Er}(\text{Et-bzimpy})_3](\text{ClO}_4)_3$ (30 K), b) $[\text{Er}(\text{tpy})_3](\text{ClO}_4)_3$ (105 K), c) $(\text{HNEt}_3)_5[\text{Er}(\text{dpa})_3](\text{CF}_3\text{SO}_3)_2$ (60 K), d) $[\text{Er}(\text{dpa-ester})_3](\text{ClO}_4)_3$ (22 K) e) $[\text{Er}(\text{dpa-amide})_3](\text{ClO}_4)_3$ (183 K) in the solid state recorded upon laser excitation of the $\text{Er}(^4\text{I}_{9/2} \leftarrow ^4\text{I}_{15/2})$ transition at $\lambda_{\text{exc}} = 801$ nm ($\tilde{\nu}_{\text{exc}} = 12284$ cm⁻¹). The blank (red curve) was recorded upon irradiation of the copper plate support covered with silver glue at maximum intensity $P = 29$ W cm⁻². f) Corresponding log-log plot of upconverted intensities I_{up} as a function of incident pump intensities P (in W·cm⁻²).

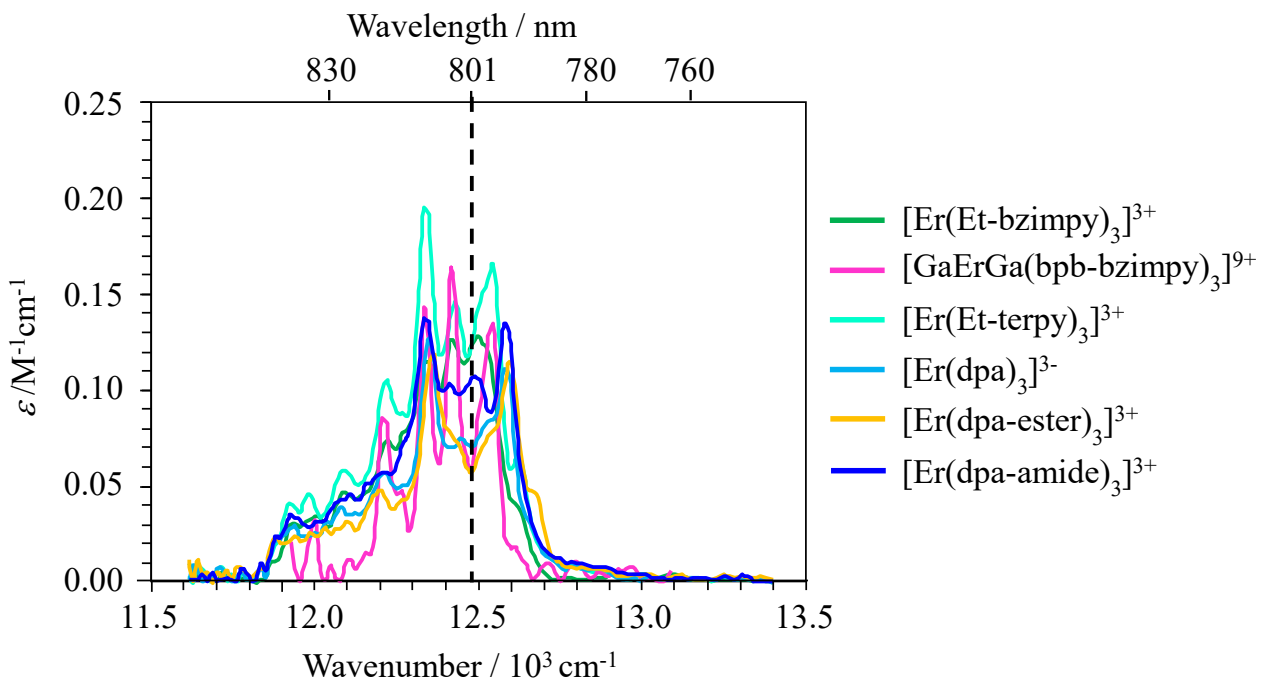


Figure S19 Absorption spectra showing the $\text{Er}(4\text{I}_{9/2} \leftarrow 4\text{I}_{15/2})$ transition in $[\text{Er}(\text{L})_3]^{3+}$ ($\text{L} = \text{Et-bzimpy, Et-tpy, tpy dpa-amide, dpa-ester}$) and $[\text{Er}(\text{dpa})_3]^{3-}$ (10 mM in acetonitrile at 298 K).

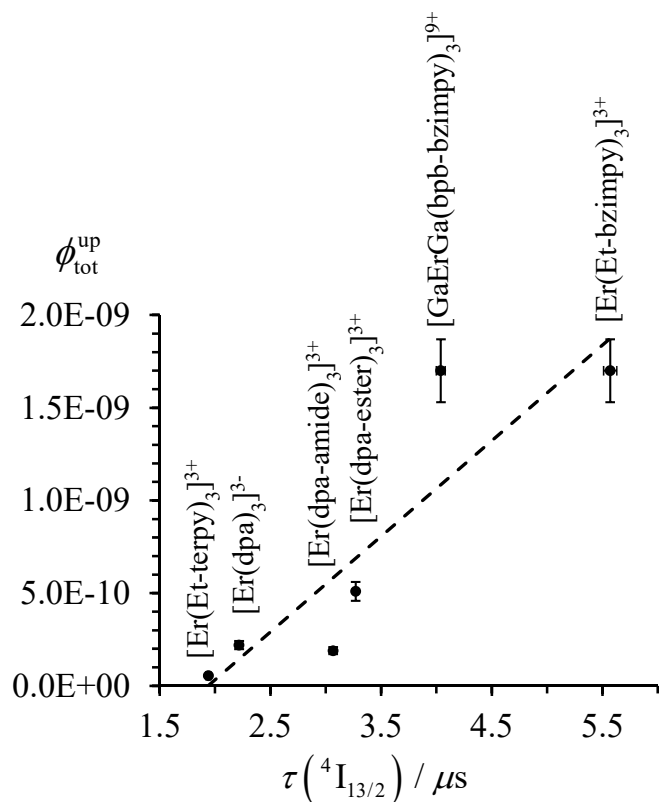


Figure S20 Upconverted quantum yield plotted as a function of the exited lifetime of the intermediate $\text{Er}(4\text{I}_{13/2})$ level for $[\text{GaErGa(bp}_b\text{-bzimpy)}_3]^{9+}$, $[\text{Er}(\text{L})_3]^{3+}$ ($\text{L} = \text{Et-bzimpy, Et-tpy, tpy dpa-amide, dpa-ester}$) and $[\text{Er}(\text{dpa})_3]^{3-}$ (10 mM in acetonitrile at 298 K). The dashed line is only a guide for the eyes.

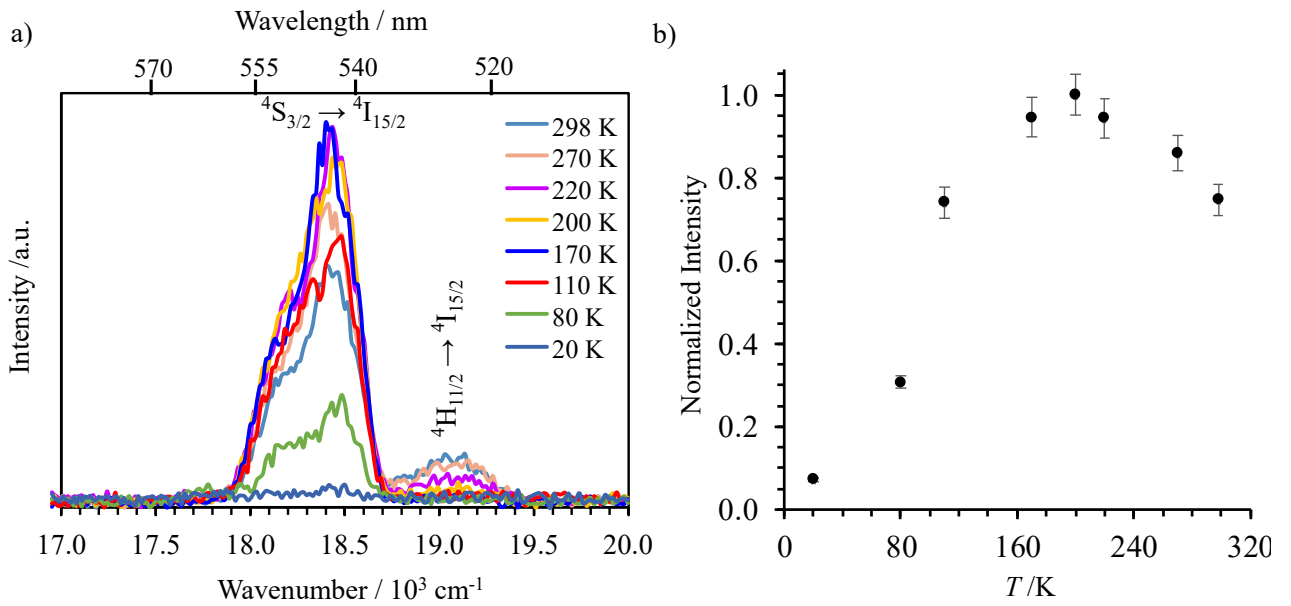


Figure S21 a) Upconverted visible $\text{Er}(^2\text{H}_{11/2} \rightarrow {}^4\text{I}_{15/2})$ and $\text{Er}(^4\text{S}_{3/2} \rightarrow {}^4\text{I}_{15/2})$ emissions observed for $[\text{GaErGa}(\text{bpdbzimpy})_3](\text{CF}_3\text{SO}_3)_9$ in the solid state ($P = 29 \text{ W}\cdot\text{cm}^{-2}$) upon laser excitation of the $\text{Er}(^4\text{I}_{9/2} \leftarrow {}^4\text{I}_{15/2})$ transition at $\lambda_{\text{exc}} = 801 \text{ nm}$ ($\tilde{\nu}_{\text{exc}} = 12284 \text{ cm}^{-1}$) at variable temperatures and b) dependence of upconverted intensities I as a function of temperature.

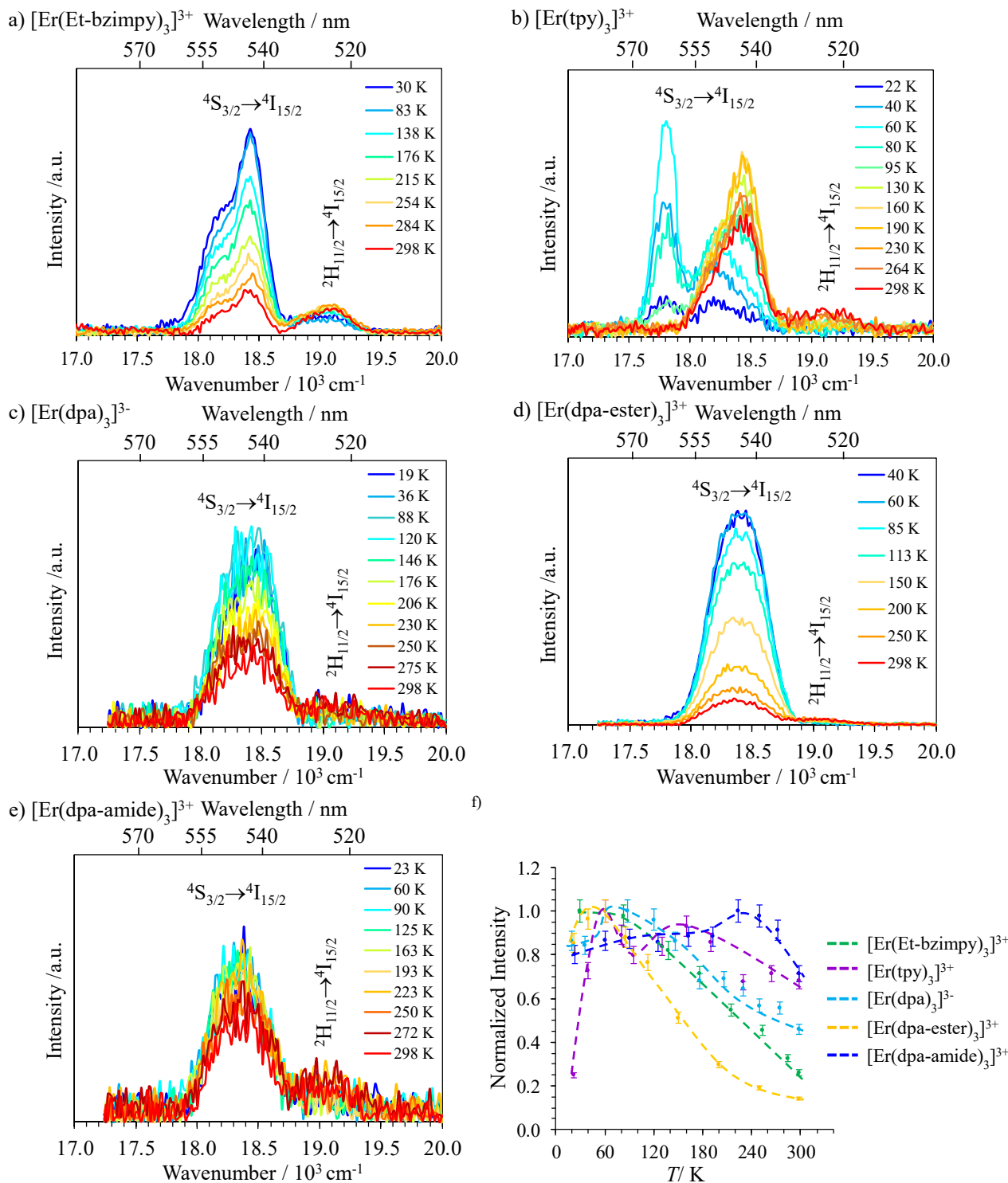


Figure S22 Upconverted visible Er($^2H_{11/2} \rightarrow ^4I_{15/2}$) and Er($^4S_{3/2} \rightarrow ^4I_{15/2}$) emissions observed for a) $[Er(Et\text{-bzimpy})_3](ClO_4)_3$, b) $[Er(tpy)_3](ClO_4)_3$, c) $(HNEt_3)_5[Er(dpa)_3](CF_3SO_3)_2$, d) $[Er(dpa\text{-ester})_3](ClO_4)_3$ and e) $[Er(dpa\text{-amide})_3](ClO_4)_3$ in the solid state ($P = 14\text{--}29\text{ W}\cdot\text{cm}^{-2}$) upon laser excitation of the $Er(^4I_{9/2} \leftarrow ^4I_{15/2})$ transition at $\lambda_{exc} = 801\text{ nm}$ ($\tilde{\nu}_{exc} = 12284\text{ cm}^{-1}$) and for different temperatures and f) associated dependences of the Er-centered upconverted emission intensity as a function of temperature (the dashed lines are only guides for the eyes).

Table S16. Oscillator strengths f ($\times 10^{-8}$) computed for the $\text{Er}({}^{2S+1}L_J \leftarrow {}^4\text{I}_{15/2})$ transitions with SO-CASSCF(PT2shift) in $[\text{Er}(\mathbf{L})_3]^{3+}$ (\mathbf{L} = Et-bzimpy, Et-tpy, dpa-amide, dpa-ester) and $[\text{Er}(\text{dpa})_3]^{3-}$.^a

Compound		${}^4\text{I}_{13/2}$	${}^4\text{I}_{11/2}$	${}^4\text{I}_{9/2}$	${}^4\text{F}_{9/2}$	${}^4\text{S}_{3/2}$	${}^2\text{H}_{11/2}$	${}^4\text{F}_{7/2}$	${}^4\text{F}_{3/2}$
$[\text{Er}(\text{Et-bzimpy})_3]^{3+}$	Energy min /cm ⁻¹ ^b	6685	10676	13040	17203	21212	21597	23062	25186
	Energy max /cm ⁻¹	6817	10742	13236	17285	21232	21666	23165	25230
	f (ED) ^c	1120	441	4.4	751	615	131	1140	379
	f (EQ)	$1.25 \cdot 10^{-1}$	$7.6 \cdot 10^{-2}$	$5.9 \cdot 10^{-4}$	$9.0 \cdot 10^{-3}$	$1.4 \cdot 10^{-2}$	6.2	$1.4 \cdot 10^{-2}$	$2.4 \cdot 10^{-3}$
	f (MD)	2040	$6.7 \cdot 10^{-1}$	$7.0 \cdot 10^{-2}$	$3.5 \cdot 10^{-1}$	$1.1 \cdot 10^{-1}$	$2.1 \cdot 10^{-1}$	$2.7 \cdot 10^{-1}$	$4.4 \cdot 10^{-2}$
	f (total)	3160	442	4.4	751	615	137	1140	379
$[\text{Er}(\text{tpy})_3]^{3+}$	Energy min /cm ⁻¹	6671	10661	13023	17201	21203	21587	23071	25184
	Energy max /cm ⁻¹	6800	10726	13229	17272	21222	21658	23162	25220
	f (ED)	1280	504	5.4	881	698	148	1270	388
	f (EQ)	$1.3 \cdot 10^{-1}$	$7.8 \cdot 10^{-2}$	$7.5 \cdot 10^{-4}$	$1.0 \cdot 10^{-2}$	$1.4 \cdot 10^{-2}$	6.4	$1.6 \cdot 10^{-2}$	$3.1 \cdot 10^{-3}$
	f (MD)	2210	$7.5 \cdot 10^{-1}$	8.5E-02	$4.1 \cdot 10^{-1}$	$1.4 \cdot 10^{-1}$	$2.7 \cdot 10^{-1}$	$3.3 \cdot 10^{-1}$	$7.2 \cdot 10^{-2}$
	f (total)	3490	505	5.5	881	698	155	1270	388
$[\text{Er}(\text{dpa})_3]^{3-}$	Energy min /cm ⁻¹	6694	10688	13041	17214	21229	21615	23070	25197
	Energy max /cm ⁻¹	6849	10769	13268	17315	21254	21698	23196	25253
	f (ED)	1110	434	3.6	709	605	129	1070	379
	f (EQ)	$1.2 \cdot 10^{-1}$	$7.1 \cdot 10^{-2}$	$7.3 \cdot 10^{-4}$	$1.0 \cdot 10^{-2}$	$2.5 \cdot 10^{-2}$	5.8	$1.3 \cdot 10^{-2}$	$2.7 \cdot 10^{-3}$
	f (MD)	2130	$8.5 \cdot 10^{-1}$	$9.6 \cdot 10^{-2}$	$4.9 \cdot 10^{-1}$	$1.1 \cdot 10^{-1}$	$3.3 \cdot 10^{-1}$	$3.4 \cdot 10^{-1}$	$4.0 \cdot 10^{-2}$
	f (total)	3240	435	3.7	710	605	135	1070	379

[Er(dpa-ester) ₃] ³⁺	Energy min /cm ⁻¹	6691	10690	13031	17234	21237	21610	23093	25226
	Energy max /cm ⁻¹	6836	10756	13266	17301	21244	21691	23183	25240
	f (ED)	1150	447	5.6	792	621	143	1130	372
	f (EQ)	$1.2 \cdot 10^{-1}$	$7.1 \cdot 10^{-2}$	$7.4 \cdot 10^{-4}$	$9.3 \cdot 10^{-3}$	$1.9 \cdot 10^{-2}$	5.8	$1.4 \cdot 10^{-2}$	$2.8 \cdot 10^{-3}$
	f (MD)	1950	$9.4 \cdot 10^{-1}$	$1.1 \cdot 10^{-1}$	$4.9 \cdot 10^{-1}$	$1.4 \cdot 10^{-1}$	$2.8 \cdot 10^{-1}$	$3.8 \cdot 10^{-1}$	$5.2 \cdot 10^{-2}$
	f (total)	3100	448	5.7	793	621	149	1130	372
[Er(dpa-amide) ₃] ³⁺	Energy min /cm ⁻¹	6681	10674	13027	17214	21220	21596	23076	25201
	Energy max /cm ⁻¹	6826	10749	13246	17308	21237	21680	23173	25231
	f (ED)	1120	447	3.5	722	590	126	1080	371
	f (EQ)	$1.3 \cdot 10^{-1}$	$7.4 \cdot 10^{-2}$	$7.9 \cdot 10^{-4}$	$1.1 \cdot 10^{-2}$	$3.1 \cdot 10^{-2}$	6.1	$1.4 \cdot 10^{-2}$	$2.5 \cdot 10^{-3}$
	f (MD)	2170	$7.9 \cdot 10^{-1}$	$9.7 \cdot 10^{-2}$	$4.6 \cdot 10^{-1}$	$1.2 \cdot 10^{-1}$	$2.7 \cdot 10^{-1}$	$3.3 \cdot 10^{-1}$	$4.1 \cdot 10^{-2}$
	f (total)	3290	448	3.6	722	590	132	1080	371

^a The oscillator strength $f_{m,n}$ between two spectroscopic levels correspond to the sum over the all possible transitions between the crystal-field m,n sublevels of the Er($^{2S+1}L_J \leftarrow ^4I_{15/2}$) transitions weighted by the Boltzmann distribution of the split $^4I_{15/2}$ spectroscopic level. ^b Computed for the lower, respectively higher crystal field sublevel of the $^{2S+1}L_J$ spectroscopic level with respect to the lowest crystal-field sublevel of the starting $^4I_{15/2}$ spectroscopic level. ^c ED = electric dipole, EQ = electric quadrupole and MD = magnetic dipole.

Table S17. Oscillator strengths f ($\times 10^{-8}$) computed for the $\text{Er}({}^{2S+1}L_J \leftarrow {}^4\text{I}_{13/2})$ transitions with SO-CASSCF(PT2shift) in $[\text{Er}(\mathbf{L})_3]^{3+}$ (\mathbf{L} = Et-bzimpy, Et-tpy, dpa-amide, dpa-ester) and $[\text{Er}(\text{dpa})_3]^{3-}$.^a

Compound		${}^4\text{I}_{11/2}$	${}^4\text{I}_{9/2}$	${}^4\text{F}_{9/2}$	${}^4\text{S}_{3/2}$	${}^2\text{H}_{11/2}$	${}^4\text{F}_{7/2}$	${}^4\text{F}_{3/2}$	${}^4\text{F}_{5/2}$
$[\text{Er}(\text{Et-bzimpy})_3]^{3+}$	Energy min /cm ⁻¹ ^b	10676	13040	17203	21212	21597	23062	25186	25306
	Energy max /cm ⁻¹	10742	13236	17285	21232	21666	23165	25230	25343
	f (ED) ^c	636	525	274	748	161	24	156	836
	f (EQ)	$1.5 \cdot 10^{-1}$	$4.0 \cdot 10^{-3}$	$7.4 \cdot 10^{-2}$	$4.9 \cdot 10^{-3}$	$1.7 \cdot 10^{-1}$	$3.5 \cdot 10^{-3}$	$2.0 \cdot 10^{-3}$	$7.4 \cdot 10^{-3}$
	f (MD)	2080	1.7	$3.2 \cdot 10^{-1}$	1.6	1130	$7.9 \cdot 10^{-1}$	$3.4 \cdot 10^{-2}$	$3.6 \cdot 10^{-1}$
	f (total)	2716	527	274	750	1291	25	156	836
$[\text{Er}(\text{tpy})_3]^{3+}$	Energy min /cm ⁻¹	10661	13023	17201	21203	21587	23071	25184	25304
	Energy max /cm ⁻¹	10726	13229	17272	21222	21658	23162	25220	25333
	f (ED)	671	552	294	779	173	33	129	914
	f (EQ)	$1.4 \cdot 10^{-1}$	$4.2 \cdot 10^{-3}$	$7.2 \cdot 10^{-2}$	$5.1 \cdot 10^{-3}$	$1.7 \cdot 10^{-1}$	$3.8 \cdot 10^{-3}$	$2.3 \cdot 10^{-3}$	$7.6 \cdot 10^{-3}$
	f (MD)	1860	1.9	$3.0 \cdot 10^{-1}$	1.8	1140	1.1	$5.5 \cdot 10^{-2}$	$3.8 \cdot 10^{-1}$
	f (total)	2531	554	294	781	1313	34	129	914
$[\text{Er}(\text{dpa})_3]^{3-}$	Energy min /cm ⁻¹	10688	13041	17214	21229	21615	23070	25197	25329
	Energy max /cm ⁻¹	10769	13268	17315	21254	21698	23196	25253	25374
	f (ED)	639	525	271	741	160	16	191	782
	f (EQ)	$1.4 \cdot 10^{-1}$	$3.8 \cdot 10^{-3}$	$7.1 \cdot 10^{-2}$	$5.0 \cdot 10^{-3}$	$1.6 \cdot 10^{-1}$	$4.4 \cdot 10^{-3}$	$2.1 \cdot 10^{-3}$	$7.8 \cdot 10^{-3}$
	f (MD)	1870	2.1	$3.8 \cdot 10^{-1}$	3.1	1040	1.1	$5.0 \cdot 10^{-2}$	$4.1 \cdot 10^{-1}$
	f (total)	2509	527	271	744	1200	17	191	782

[Er(dpa-ester) ₃] ³⁺	Energy min /cm ⁻¹	10690	13031	17234	21237	21610	23093	25226	25335
	Energy max /cm ⁻¹	10756	13266	17301	21244	21691	23183	25240	25361
	f (ED)	643	525	279	743	164	34	134	865
	f (EQ)	$1.4 \cdot 10^{-1}$	$4.1 \cdot 10^{-3}$	$7.0 \cdot 10^{-2}$	$5.1 \cdot 10^{-3}$	$1.6 \cdot 10^{-1}$	$3.4 \cdot 10^{-3}$	$2.2 \cdot 10^{-3}$	$7.4 \cdot 10^{-3}$
	f (MD)	1700	2.3	$3.5 \cdot 10^{-1}$	2.4	933	1.1	$5.0 \cdot 10^{-2}$	$4.7 \cdot 10^{-1}$
	f (total)	2343	527	279	745	1097	35	134	865
[Er(dpa-amide) ₃] ³⁺	Energy min /cm ⁻¹	10674	13027	17214	21220	21596	23076	25201	25315
	Energy max /cm ⁻¹	10749	13246	17308	21237	21680	23173	25231	25357
	f (ED)	620	513	265	712	154	15	139	799
	f (EQ)	$1.4 \cdot 10^{-1}$	$3.9 \cdot 10^{-3}$	$7.1 \cdot 10^{-2}$	$5.1 \cdot 10^{-3}$	$1.6 \cdot 10^{-1}$	$4.5 \cdot 10^{-3}$	$2.3 \cdot 10^{-3}$	$7.9 \cdot 10^{-3}$
	f (MD)	1920	1.9	$3.5 \cdot 10^{-1}$	4.6	953	$9.5 \cdot 10^{-1}$	$6.1 \cdot 10^{-2}$	$4.1 \cdot 10^{-1}$
	f (total)	2540	515	265	717	1107	16	139	799

^a The oscillator strength $f_{m,n}$ between two spectroscopic levels correspond to the sum over the all possible transitions between the crystal-field m,n sublevels of the Er($^{2S+1}L_J \leftarrow ^4I_{13/2}$) transitions weighted by the Boltzmann distribution of the split $^4I_{13/2}$ spectroscopic level. ^b Computed for the lower, respectively higher crystal field sublevel of the $^{2S+1}L_J$ spectroscopic level with respect to the lowest crystal-field sublevel of the starting $^4I_{15/2}$ spectroscopic level. ^c ED = electric dipole, EQ = electric quadrupole and MD = magnetic dipole.

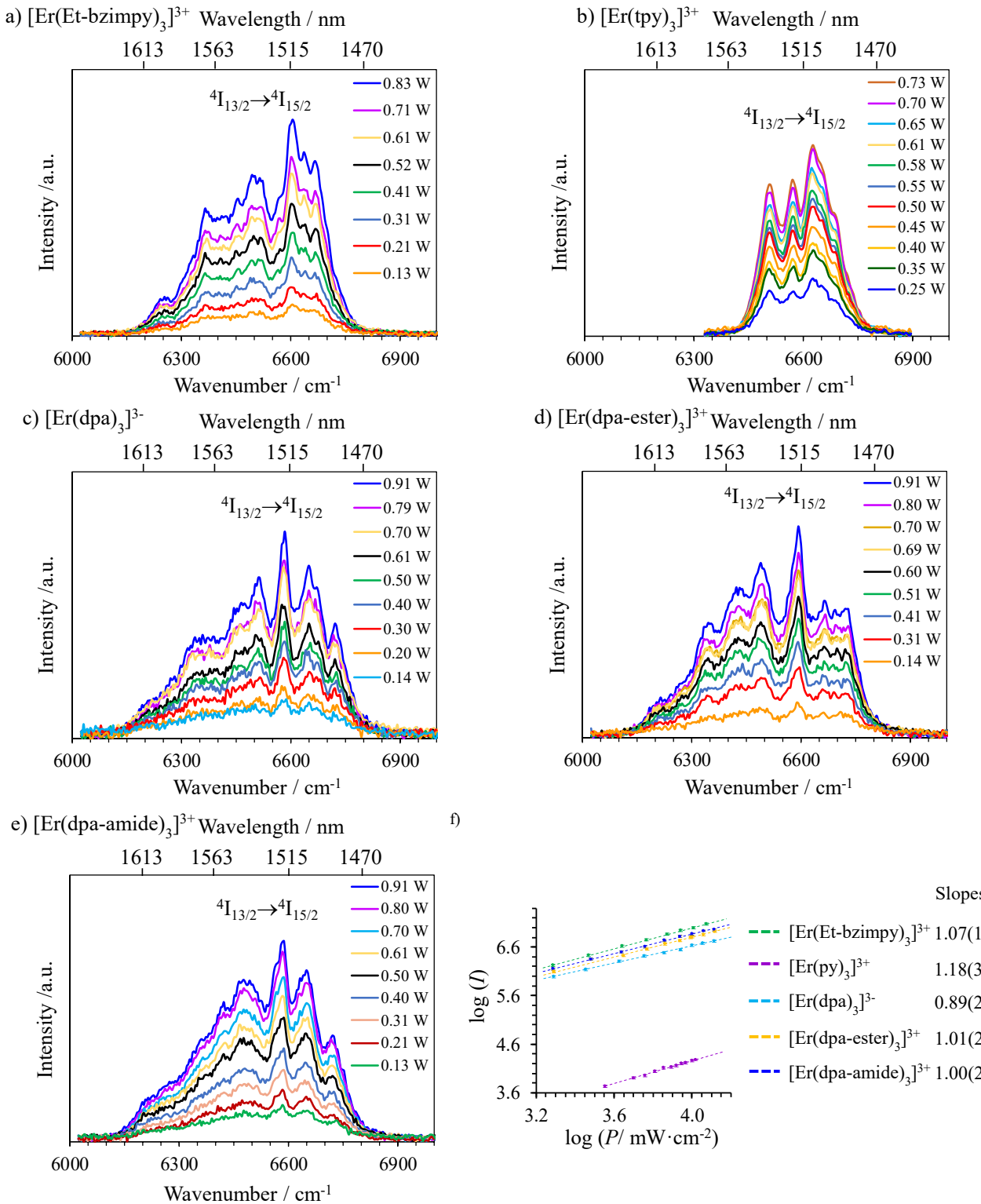


Figure S23. Near-infrared downshifted Er(${}^4\text{I}_{13/2} \rightarrow {}^4\text{I}_{15/2}$) emission observed for a) [Er(Et-bzimpy)₃](ClO₄)₃, b) [Er(tpy)₃](ClO₄)₃, c) (HNEt₃)₅[Er(dpa)₃](CF₃SO₃)₂, d) [Er(ddester)₃](ClO₄)₃ and e) [Er(ddamide)₃](ClO₄)₃ in acetonitrile (10 mM, 298 K) upon laser excitation of the Er(${}^4\text{I}_{9/2} \leftarrow {}^4\text{I}_{15/2}$) transition at $\lambda_{\text{exc}} = 801$ nm ($\tilde{\nu}_{\text{exc}} = 12284$ cm⁻¹) and for different incident pump intensities focused on a spot size of ≈ 0.07 cm² and e) corresponding log-log plots of downshifted intensities I as a function of incident pump intensities P (in mW·cm⁻²).

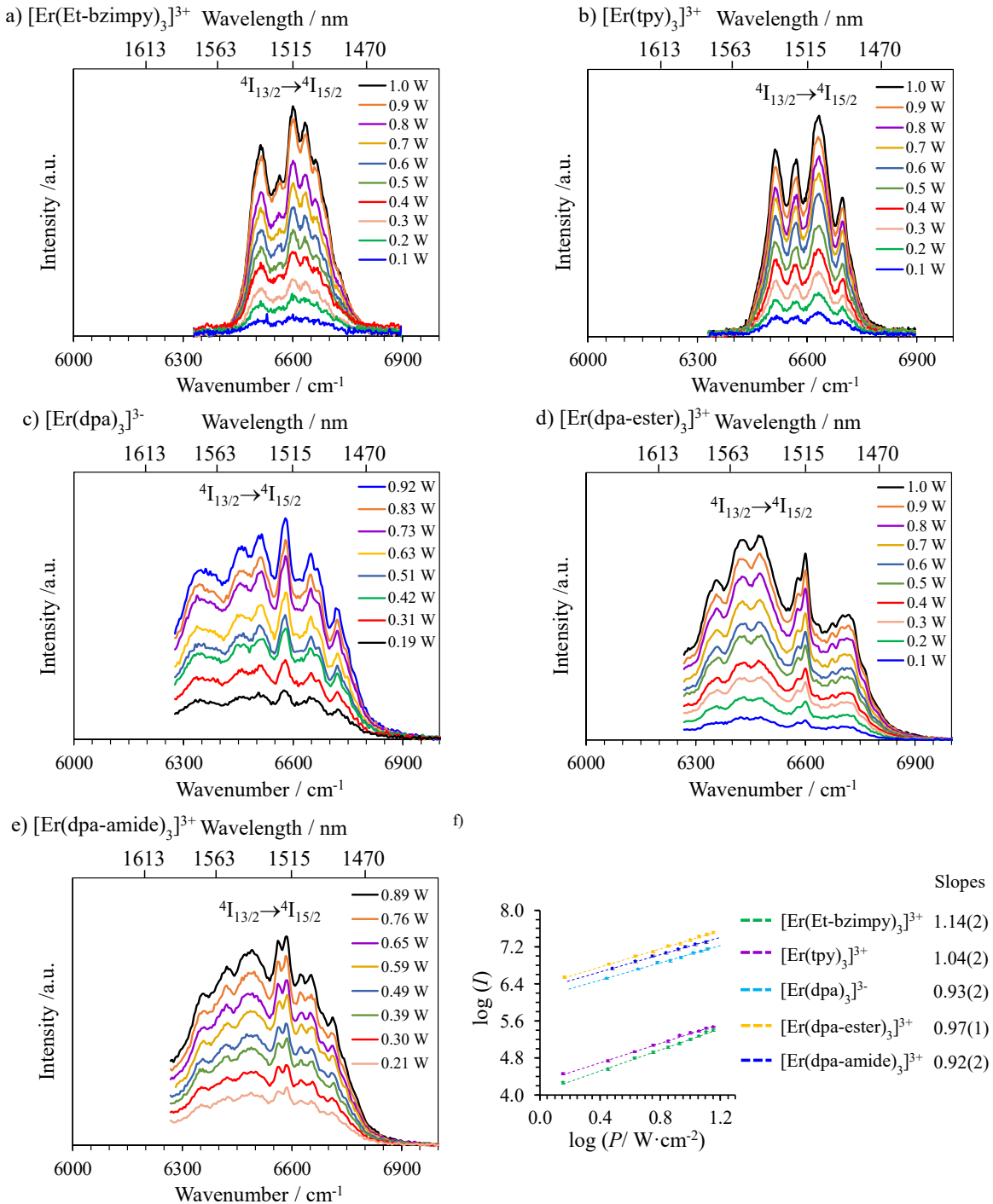


Figure S24. Near-infrared downshifted $\text{Er}({}^4\text{I}_{13/2} \rightarrow {}^4\text{I}_{15/2})$ emission observed for a) $[\text{Er}(\text{Et-bzimpy})_3](\text{ClO}_4)_3$, b) $[\text{Er}(\text{tpy})_3](\text{ClO}_4)_3$, c) $(\text{HNEt}_3)_5[\text{Er}(\text{dpa})_3](\text{CF}_3\text{SO}_3)_2$, d) $[\text{Er}(\text{ddester})_3](\text{ClO}_4)_3$ and e) $[\text{Er}(\text{ddamide})_3](\text{ClO}_4)_3$ in the solid state (298 K) upon laser excitation of the $\text{Er}({}^4\text{I}_{9/2} \leftarrow {}^4\text{I}_{15/2})$ transition at $\lambda_{\text{exc}} = 801$ nm ($\tilde{\nu}_{\text{exc}} = 12284$ cm⁻¹) and for different incident pump intensities focused on a spot size of ≈ 0.07 cm² and e) corresponding log-log plots of downshifted intensities I as a function of incident pump intensities P (in mW·cm⁻²). The collection of emission signals was stopped before the second-order Rayleigh scattering of the laser line at 1602 nm.

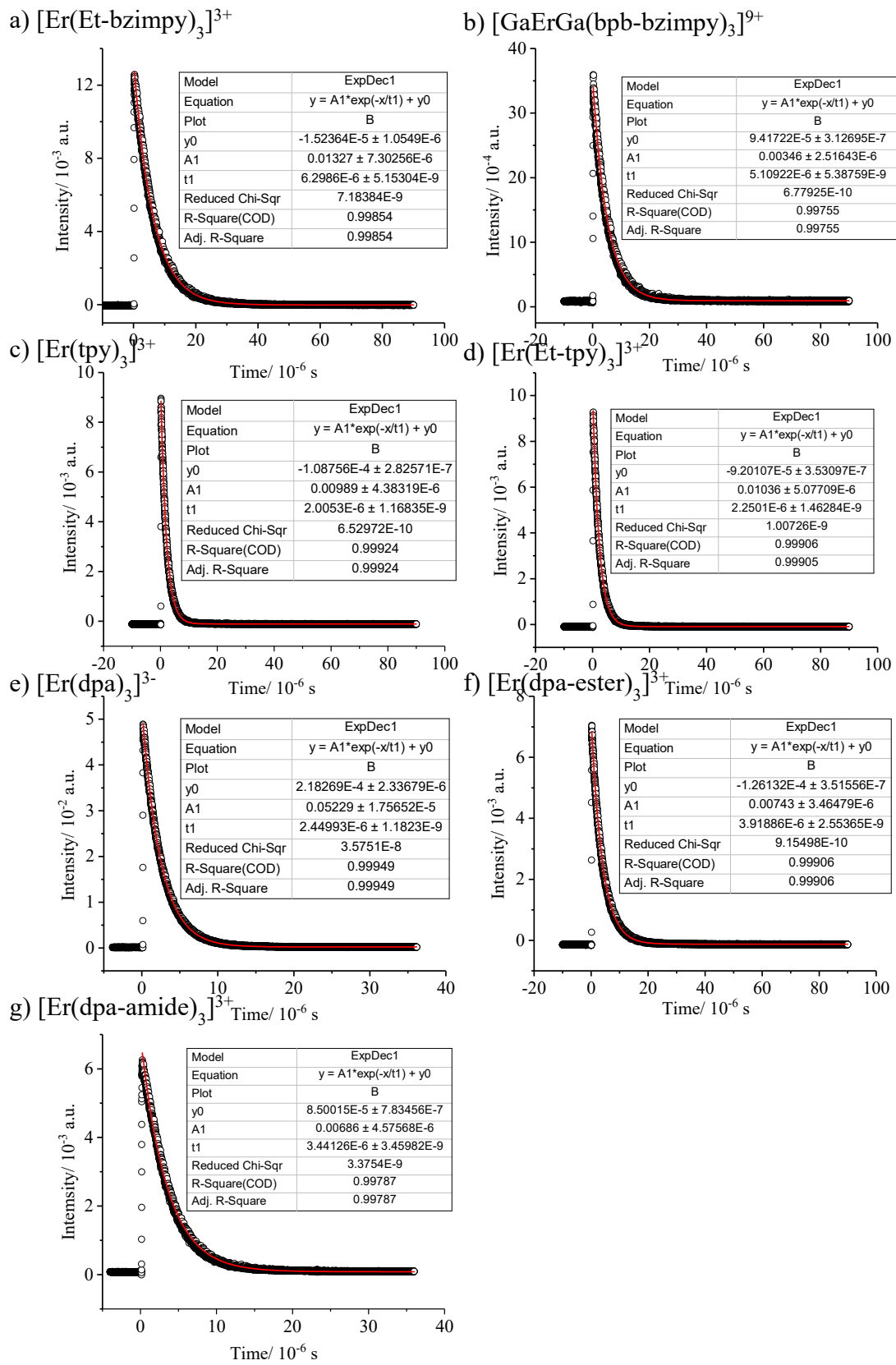


Figure S25 Decay traces of the $\text{Er}^{4\text{I}_{13/2}} \rightarrow 4\text{I}_{15/2}$ emissions observed for $[\text{GaErGa(bpb-bzimpy)}_3]^{9+}$, $[\text{Er}(\mathbf{L})_3]^{3+}$ ($\mathbf{L} = \text{Et-bzimpy, Et-tpy, tpy, dpa-amide, dpa-ester}$) and $[\text{Er(dpa)}_3]^{3-}$ in acetonitrile at 298 K recorded upon laser excitation of the $\text{Er}^{4\text{I}_{9/2}} \leftarrow 4\text{I}_{15/2}$ transition at $\lambda_{\text{exc}} = 805 \text{ nm}$ ($\tilde{\nu}_{\text{exc}} = 12422 \text{ cm}^{-1}$).

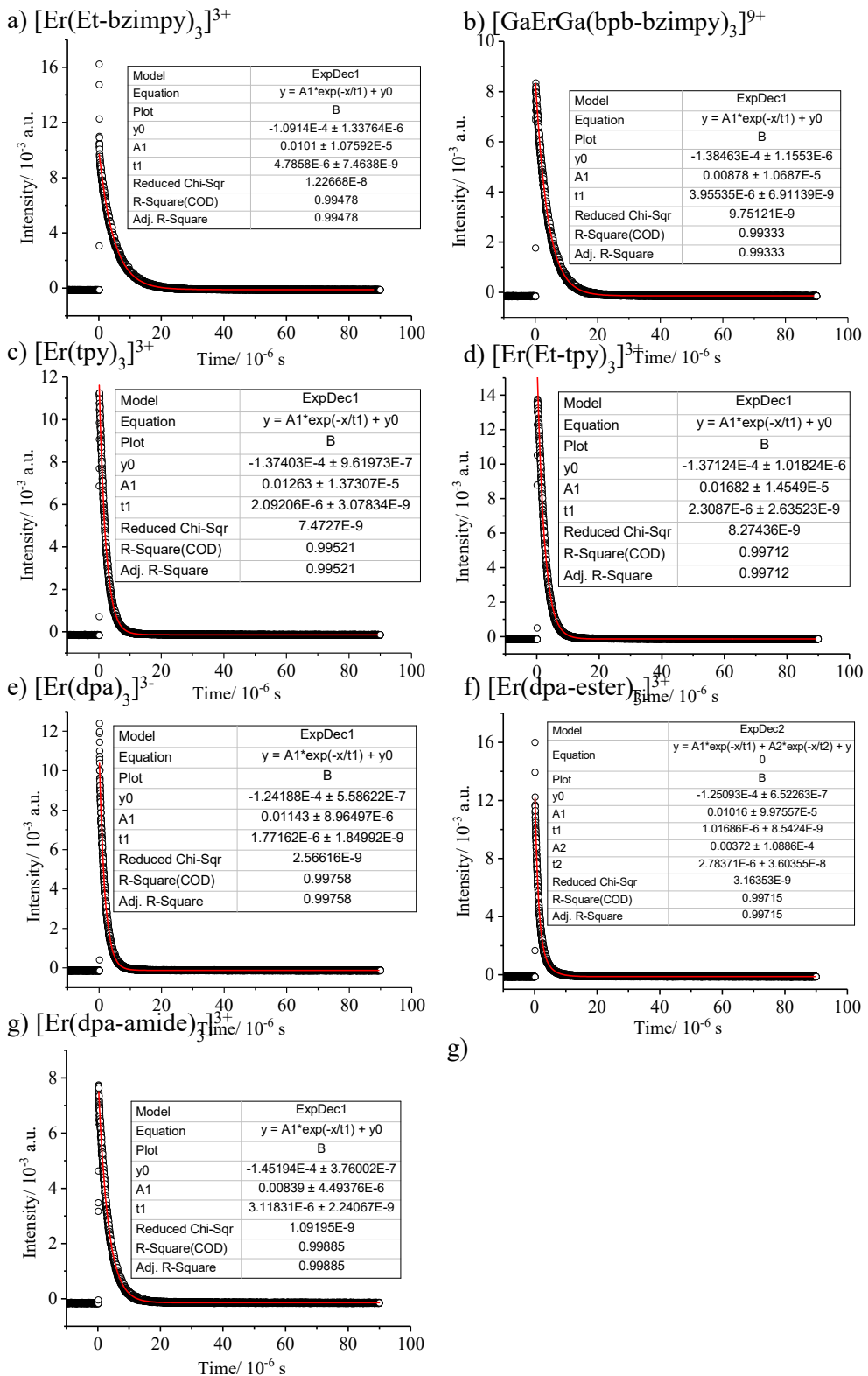


Figure S26 Decay traces of the $\text{Er}(^4\text{I}_{13/2} \rightarrow ^4\text{I}_{15/2})$ emissions observed for $(\text{NHEt}_3)_5[\text{Er(dpa)}_3](\text{CF}_3\text{SO}_3)_2$ (**1**), $[\text{Er(dpa-ester)}_3](\text{ClO}_4)_3$ (**2**), $[\text{Er(dpa-diamide)}_3](\text{ClO}_4)_3$ (**3**), $[\text{Er(Et-bzimpy)}_3](\text{ClO}_4)_3 \cdot 2\text{CH}_3\text{CN}$,^[28] $[\text{Er(tpy)}_3](\text{ClO}_4)_3$, $[\text{Er(Et-tpy)}_3](\text{ClO}_4)_3 \cdot 1.5\text{CH}_3\text{CN}$ and $[\text{GaErGa(bpb-bzimpy)}_3]_2(\text{CF}_3\text{SO}_3)_18 \cdot 30\text{C}_3\text{H}_5\text{N}$ in the solid state at 298 K recorded upon laser excitation of the $\text{Er}(^4\text{I}_{9/2} \leftarrow ^4\text{I}_{15/2})$ transition at $\lambda_{\text{exc}} = 805 \text{ nm}$ ($\tilde{\nu}_{\text{exc}} = 12422 \text{ cm}^{-1}$).

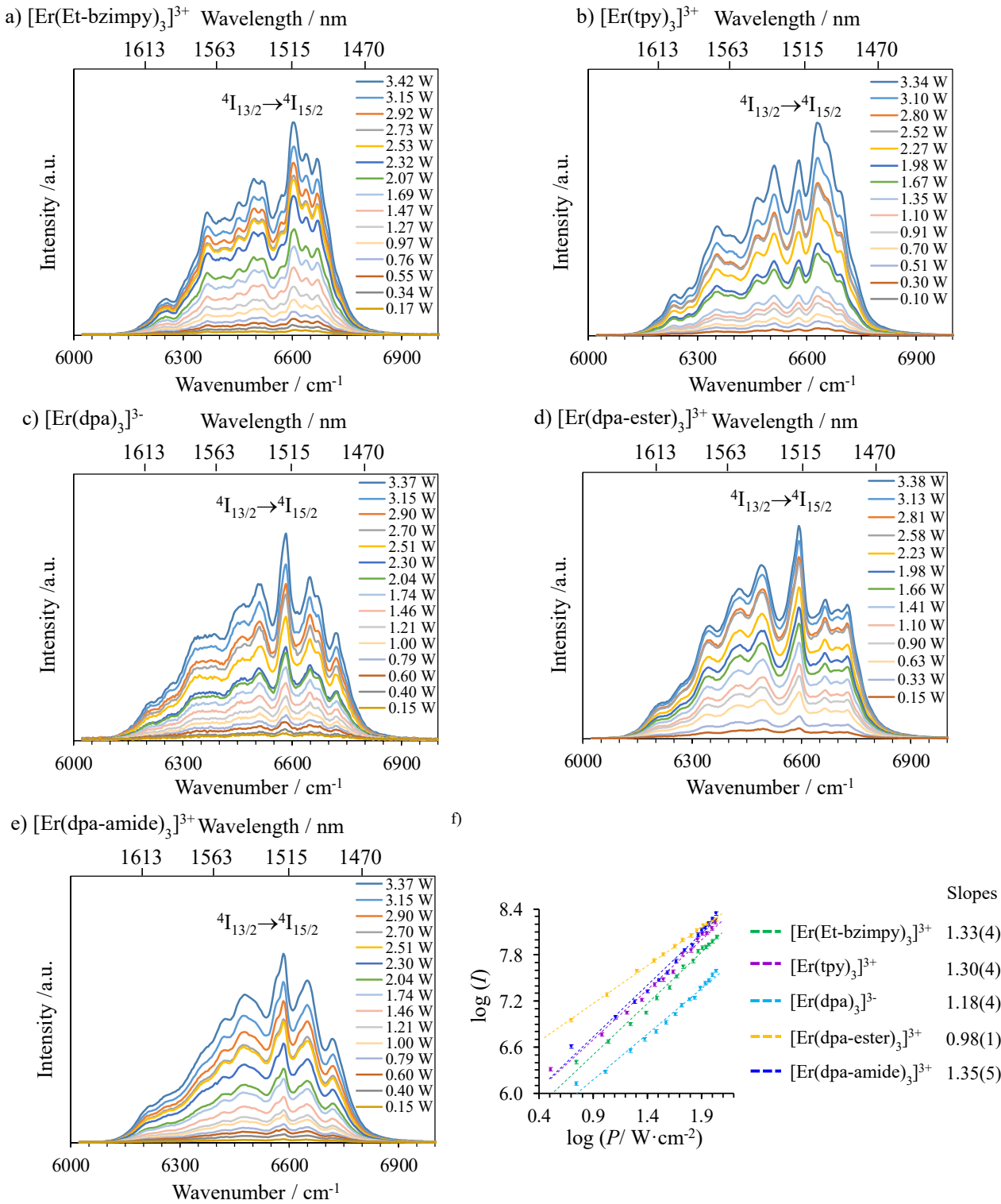


Figure S27. Near-infrared downshifted Er($^4\text{I}_{13/2} \rightarrow ^4\text{I}_{15/2}$) emission observed for a) $[\text{Er}(\text{Et-bzimpy})_3](\text{ClO}_4)_3$, b) $[\text{Er}(\text{tpy})_3](\text{ClO}_4)_3$, c) $(\text{HNEt}_3)_5[\text{Er}(\text{dpa})_3](\text{CF}_3\text{SO}_3)_2$, d) $[\text{Er}(\text{ddester})_3](\text{ClO}_4)_3$ and e) $[\text{Er}(\text{ddamide})_3](\text{ClO}_4)_3$ in acetonitrile (10 mM, 298 K) upon laser excitation of the Er($^4\text{I}_{11/2} \leftarrow ^4\text{I}_{15/2}$) transition at $\lambda_{\text{exc}} = 975$ nm ($\tilde{\nu}_{\text{exc}} = 10256$ cm⁻¹) and for different incident pump intensities focused on a spot size of ≈ 0.07 cm² and e) corresponding log-log plots of downshifted intensities I as a function of incident pump intensities P (in W·cm⁻²).

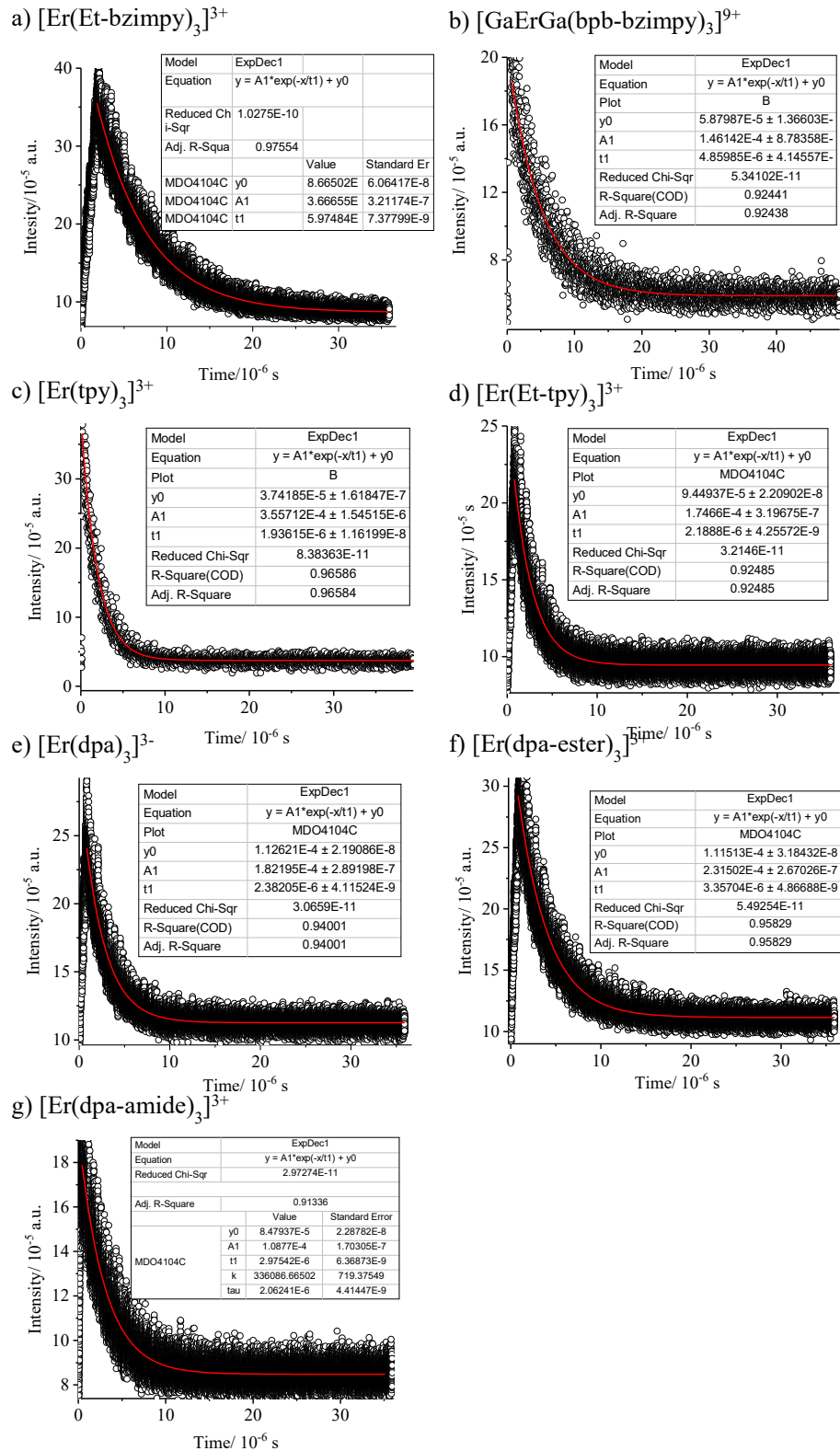


Figure S28 Decay traces of the $\text{Er}(4\text{I}_{13/2} \rightarrow 4\text{I}_{15/2})$ emissions observed for $[\text{GaErGa(bpb-bzimpy)}_3]^{9+}$, $[\text{Er(L)}_3]^{3+}$ ($\text{L} = \text{Et-bzimpy, Et-tpy, tpy, dpa-amide, dpa-ester}$) and $[\text{Er(dpa)}_3]^{3-}$ in acetonitrile at 298 K recorded upon laser excitation of the $\text{Er}(4\text{I}_{11/2} \leftarrow 4\text{I}_{15/2})$ transition at $\lambda_{\text{exc}} = 975$ nm ($\tilde{\nu}_{\text{exc}} = 10256 \text{ cm}^{-1}$).

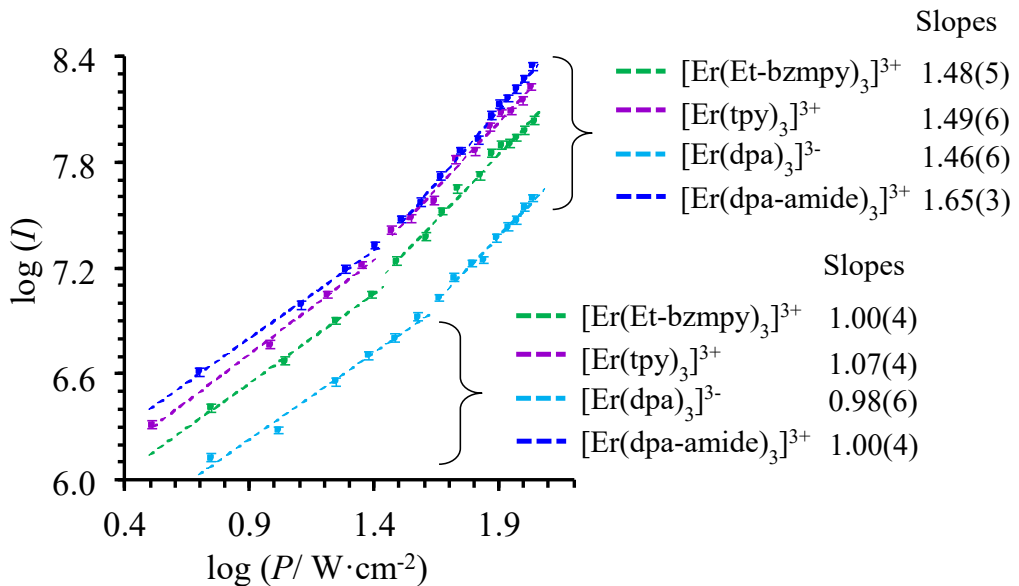
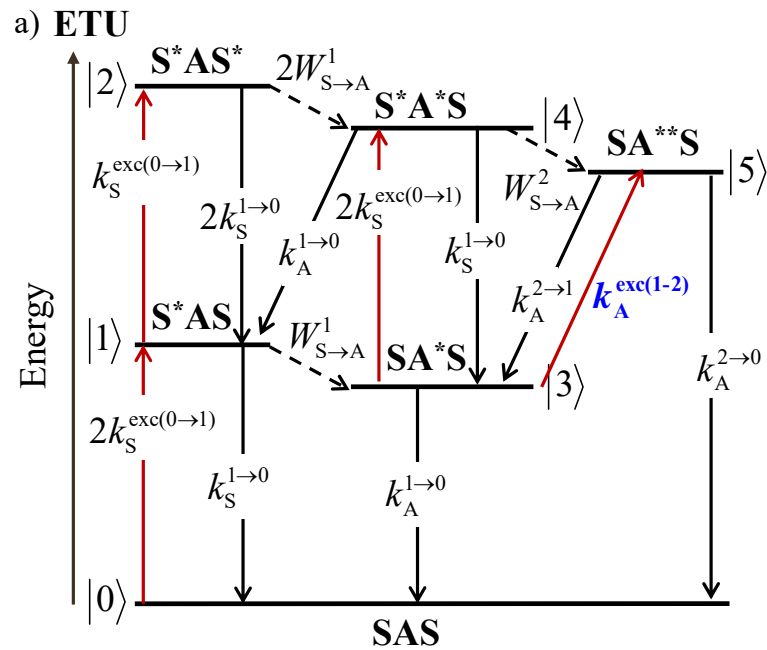


Figure S29 Log-log plots of downshifted intensities I as a function of incident pump intensities P (in $\text{W}\cdot\text{cm}^{-2}$) observed for $[\text{Er}(\mathbf{L})_3]^{3+}$ ($\mathbf{L} = \text{Et-bzimpy, tpy, dpa-amide}$) and $[\text{Er}(\text{dpa})_3]^{3-}$ recorded upon laser excitation of the $\text{Er}({}^4\text{I}_{11/2} \leftarrow {}^4\text{I}_{15/2})$ transition at $\lambda_{\text{exc}} = 966$ nm ($\tilde{\nu}_{\text{exc}} = 10350$ cm^{-1}) in acetonitrile solution at 298 K ($c = 10$ mM).



b)

$$\phi_{\text{tot}}^{\text{up}} = \left[\left(\frac{W_{S \rightarrow A}^1}{W_{S \rightarrow A}^1 + k_S^{1 \rightarrow 0} + k_S^{\text{exc}(0 \rightarrow 1)}} \right) \left(\frac{2k_S^{\text{exc}(0 \rightarrow 1)}}{2k_S^{\text{exc}(0 \rightarrow 1)} + k_A^{1 \rightarrow 0} + k_A^{\text{exc}(1 \rightarrow 2)}} \right) \left(\frac{W_{S \rightarrow A}^2}{W_{S \rightarrow A}^2 + k_S^{1 \rightarrow 0} + k_A^{1 \rightarrow 0}} \right) \right] \times \left(\frac{k_A^{2 \rightarrow 0}}{k_A^{2 \rightarrow 0} + k_A^{2 \rightarrow 1}} \right) = \eta_{\text{ETU}} \phi_A$$

$$+ \left(\frac{k_S^{\text{exc}(0 \rightarrow 1)}}{W_{S \rightarrow A}^1 + k_S^{1 \rightarrow 0} + k_S^{\text{exc}(0 \rightarrow 1)}} \right) \left(\frac{2W_{S \rightarrow A}^1}{2W_{S \rightarrow A}^1 + 2k_S^{1 \rightarrow 0}} \right) \left(\frac{W_{S \rightarrow A}^2}{W_{S \rightarrow A}^2 + k_S^{1 \rightarrow 0} + k_A^{1 \rightarrow 0}} \right)$$

$$+ \left(\frac{W_{S \rightarrow A}^1}{W_{S \rightarrow A}^1 + k_S^{1 \rightarrow 0} + k_S^{\text{exc}(0 \rightarrow 1)}} \right) \left(\frac{k_A^{\text{exc}(1 \rightarrow 2)}}{2k_S^{\text{exc}(0 \rightarrow 1)} + k_A^{1 \rightarrow 0} + k_A^{\text{exc}(1 \rightarrow 2)}} \right)$$

Figure S30 a) Kinetic scheme depicting the modelling of the Sensitizer/Activator energy transfer upconversion (ETU) process occurring upon off-resonance irradiation into the sensitizer-centered absorption band in a SAS system with contribution of an activator-centered ESA mechanism (highlighted in blue). b) Modeling of the upconversion quantum yield ($\phi_{\text{tot}}^{\text{up}}$) obtained under steady-state (S-S) excitation for the mixed ETU/ESA mechanism depicted in Fig. S28a.